A&A 582, A14 (2015)
DOI: 10.1051/0004-6361/201425582

Astronomy & Astrophysics

Stellar populations of galaxies in the ALHAMBRA survey up to $z \sim 1$

I. MUFFIT: A multi-filter fitting code for stellar population diagnostics

L. A. Díaz-García[1], A. J. Cenarro[1], C. López-Sanjuan[1], I. Ferreras[2], J. Varela[1], K. Viironen[1], D. Cristóbal-Hornillos[1], M. Moles[1,3], A. Marín-Franch[1], P. Arnalte-Mur[4], B. Ascaso[5,3], M. Cerviño[3,6,7], R. M. González Delgado[3], I. Márquez[3], J. Masegosa[3], A. Molino[8,3], M. Pović[3], E. Alfaro[3], T. Aparicio-Villegas[9,3], N. Benítez[3], T. Broadhurst[10,11], J. Cabrera-Caño[12], F. J. Castander[13], J. Cepa[6,7], A. Fernández-Soto[14,15], C. Husillos[3], L. Infante[16], J. A. L. Aguerri[6,7], V. J. Martínez[4,17,15], A. del Olmo[3], J. Perea[3], F. Prada[3,18,19], J. M. Quintana[3], and N. Gruel[20]

(Affiliations can be found after the references)

Received 24 December 2014 / Accepted 26 May 2015

ABSTRACT

Aims. We present MUFFIT, a new generic code optimized to retrieve the main stellar population parameters of galaxies in photometric multi-filter surveys, and check its reliability and feasibility with real galaxy data from the ALHAMBRA survey.
Methods. Making use of an error-weighted χ^2-test, we compare the multi-filter fluxes of galaxies with the synthetic photometry of mixtures of two single stellar populations at different redshifts and extinctions, to provide the most likely range of stellar population parameters (mainly ages and metallicities), extinctions, redshifts, and stellar masses. To improve the diagnostic reliability, MUFFIT identifies and removes from the analysis those bands that are significantly affected by emission lines. The final parameters and their uncertainties are derived by a Monte Carlo method, using the individual photometric uncertainties in each band. Finally, we discuss the accuracies, degeneracies, and reliability of MUFFIT using both simulated and real galaxies from ALHAMBRA, comparing with results from the literature.
Results. MUFFIT is a precise and reliable code to derive stellar population parameters of galaxies in ALHAMBRA. Using the results from photometric-redshift codes as input, MUFFIT improves the photometric-redshift accuracy by ~10–20%. MUFFIT also detects nebular emissions in galaxies, providing physical information about their strengths. The stellar masses derived from MUFFIT show excellent agreement with the COSMOS and SDSS values. In addition, the retrieved age-metallicity locus for a sample of $z \leq 0.22$ early-type galaxies in ALHAMBRA at different stellar mass bins are in very good agreement with the ones from SDSS spectroscopic diagnostics. Moreover, a one-to-one comparison between the redshifts, ages, metallicities, and stellar masses derived spectroscopically for SDSS and by MUFFIT for ALHAMBRA reveals good qualitative agreements in all the parameters, hence reinforcing the strengths of multi-filter galaxy data and optimized analysis techniques, like MUFFIT, to conduct reliable stellar population studies.

Key words. galaxies: stellar content – galaxies: photometry – galaxies: evolution – galaxies: formation – galaxies: high-redshift

1. Introduction

Studying the stellar content of galaxies is crucial to understanding their star formation histories (SFH), which in turn provides us with valuable information about the possible evolutive paths from their formation at high redshift down to the present time. Despite the strong efforts and advances achieved in this topic during the past decades, it still remains as one of the most challenging and promising ways to understand galaxy evolution.

Early attempts to study the stellar content of early-type galaxies were based on colours from wide and narrow band photometry (Baum 1959; Tifft 1963; Wood 1966; McClure & van den Bergh 1968; Faber 1973) and on empirical synthesis of the populations using the observed colours of nearby early-types as basis. These early methods can be considered as the pioneers of the current photo-spectral fitting techniques, which are the main topic of the present paper. The above methods were gradually displaced by techniques based in more specific features (Faber 1973; Pritchet 1977) that were defined in narrow spectral ranges.

The arrival of absorption line-strength indices to study the stellar content of galaxies (Burstein et al. 1984; Faber et al. 1985) brought a significant breakthrough in the field. On this front, it is worth noting the Lick system of indices (Gorgas et al. 1993; Worthey et al. 1994), which for the past decades has been the standard for most spectroscopic studies in stellar populations in the optical (e.g. Trager et al. 1998; Jørgensen 1999; Kuntschner et al. 2001; Thomas et al. 2005; Bernardi et al. 2006; Sánchez-Blázquez et al. 2006a; Gorgas et al. 2007). The combination of a certain number of absorption lines mainly sensitive to age, such as the Balmer lines, or to the metallicity, as traced by certain elements such as Fe , Mg , Ti , C , Ca , and Na , were proven to be an efficient way to break the well known degeneracy between these two parameters, at least to some extent (Worthey 1994). The way to measure these features is delicately chosen to be very sensitive to a parameter of interest, focusing its study on narrow spectral ranges. By construction, line-strength indices are quite insensitive to the influence of extinction, and by fine-tuning their definition or combining the sensitivities of different indices, some of them may end up being almost independent of other parameters, such as metallicity (Vazdekis & Arimoto 1999; Cervantes & Vazdekis 2009) and α-element overabundances (Thomas et al. 2003).

In the past fifteen years, the development of stellar libraries in spectral ranges other than the optical has driven the definition of new indices that allowed this kind of study to be extended to

other regions with unexplored sensitivities (Cenarro et al. 2002; Mármol-Queraltó et al. 2008). In addition, the index system of reference in the optical spectral range has been revisited and improved (see e.g. Vazdekis et al. 2010) thanks to the availability of much better stellar libraries at much better spectral resolution.

It was with the arrival of improved stellar libraries, such as CaT (Cenarro et al. 2001a,b), ELODIE (Prugniel & Soubiran 2001), STELIB (Le Borgne et al. 2003), INDO-US (Valdes et al. 2004), Martins et al. (2005), and MILES (Sánchez-Blázquez et al. 2006b; Cenarro et al. 2007), and the consequent evolutionary stellar population synthesis models (e.g. Bruzual & Charlot 2003; Vazdekis et al. 2003, 2010, 2012; González Delgado et al. 2005; Maraston et al. 2009; Conroy & van Dokkum 2012), that fitting techniques over the full spectral energy distribution (SED) of galaxies appeared as an alternative to line-strength indices. SED-fitting can also be used to derive several physical properties of galaxies (Mathis et al. 2006; Koleva et al. 2008; Coelho et al. 2009; Walcher et al. 2011; Liu et al. 2013). In fact, there is a growing number of public codes specifically devoted to carrying out SED-fitting with different procedures, such as hyperz (Bolzonella et al. 2000), Le PHARE (Arnouts et al. 2002; Ilbert et al. 2006), STARLIGHT (Cid Fernandes et al. 2005), STECKMAP (Ocvirk et al. 2006), VESPA (Tojeiro et al. 2007), ULySS (Koleva et al. 2009), FAST (Kriek et al. 2009), and SEDfit (Sawicki 2012).

Nowadays, there is an increasing number of present and future multi-filter surveys, including COMBO-17 (Wolf et al. 2003), MUSYC (Gawiser et al. 2006), COSMOS (Scoville et al. 2007), ALHAMBRA (Moles et al. 2008), CLASH (Postman et al. 2012), SHARDS (Pérez-González et al. 2013), J-PAS (Benitez et al. 2014), and J-PLUS (Cenarro et al., in prep.), each of them with a vast volume of high-quality multi-filter data. These kinds of surveys pursue diverse goals with a common feature: sampling the SEDs of galaxies using top-hat and/or broad-band filters that mainly cover the optical range. Owing to this configuration, the retrieved SEDs are half-way between classical photometry and spectroscopy, because in practice they are like a low-resolution spectrum whose resolution depends on the filter system (e.g. $R \sim 20$ for ALHAMBRA; $R \sim 50$ for J-PAS).

Although multi-filter observing techniques suffer from the lack of high spectral resolution, their advantages over standard spectroscopy are worth noting: (i) the galaxy samples of multi-filter surveys do not suffer from selection criteria other than the photometric depth in the detection band of the survey, because all the objects in the field of view are observed. For a fixed observational time and similar telescopes, this leads to much larger galaxy samples than in multi-object spectroscopy, where achieving multiplexities greater than ∼1000 is a challenge at present. (ii) Unlike standard spectroscopy, the SED of galaxies observed in multi-filter surveys does not suffer from the typical uncertainties in the flux calibration that lead to systematic colour terms, since the photometric calibration of each individual band is independent of the rest. This advantage is crucial, because it is the overall continuum of the stellar population that in most cases dominates the diagnostic with SED-fitting techniques. (iii) With similar telescopes, the depth of multi-filter surveys is usually much greater than for spectroscopic survey, since direct imaging is much more efficient than spectroscopy. (iv) Multi-filter surveys provide spatially resolved photo-spectra, similar to an integral field unit (IFU), allowing us to perform 2D stellar population studies in galaxies whose apparent sizes are not dominated by the point spread function (PSF) of the system.

It is therefore clear that multi-filter surveys open a profitable way to advance in our understanding of galaxy evolution by providing complete and homogeneous sets of galaxy SEDs down to a certain magnitude depth. Although there are several SED-fitting codes available, to cope with the calibration particularities of multi-filter surveys (see e.g. Molino et al. 2014), and given the vast amount of high-quality photometric data already available in the literature and still to come in the next years, in this paper we present MUFFIT (MUlti-Filter FITting for stellar population diagnostics), a code specifically designed for analysing the stellar content of galaxies with available multi-filter data.

This paper mainly aims to describe the code and its functionalities, set the accuracy and typical uncertainties in the retrieved stellar population parameters, and demonstrate its reliability compared with already existing stellar population results in the literature. MUFFIT was developed within the framework of the ALHAMBRA survey (see Sect. 2), so even though the code is generic and can be easily employed for any kind of photometric system, many sections in this paper are specific to the ALHAMBRA dataset. This allows us to show the code's performance on real galaxy data, which is ultimately the best sanity check for any stellar population code. Even though in this paper we use galaxy data from ALHAMBRA, it is not our intention to scientifically exploit the dataset here. In subsequent papers in this series, we will provide and exploit the stellar population parameters retrieved for the whole galaxy sample in the ALHAMBRA survey.

This paper is organized as follows. Section 2 presents a quick overview of the ALHAMBRA survey, that is, the photometric dataset employed to develop the present work. In Sect. 3, we summarise the main technical aspects of our code, MUFFIT, as well as the processes for obtaining photometric colour predictions from models of single stellar populations (SSP) and the Milky Way (MW) extinction corrections. We show the accuracy and reliability of the stellar population parameters retrieved with our code, together with the uncertainties and degeneracies expected for ALHAMBRA data in Sect. 4. Section 5 presents a comparison study of the results retrieved from ALHAMBRA galaxy data using MUFFIT with previous studies, including spectroscopic ones and data from the literature, thereby testing the reliability of our results. Finally, we provide the summary and conclusions of this research in Sect. 6.

Throughout this paper we assume a ΛCDM cosmology with $H_0 = 71$ km s^{-1}, $\Omega_M = 0.27$, and $\Omega_\Lambda = 0.73$.

2. The ALHAMBRA survey

The stellar population code that we present in this paper is generically designed for all types of multi-filter surveys. However, we make use of the data in the ALHAMBRA survey[1] to prove and test the reliability of our techniques, as in fact this code will be employed to analyse the stellar population properties of ALHAMBRA galaxies in forthcoming papers (Díaz-García et al., in prep.). Throughout this work, therefore, we mainly present results from both simulations and real observations that are based either on the ALHAMBRA data or on its technical setup. In the following paragraphs we present a short summary of the ALHAMBRA survey.

The ALHAMBRA survey provides a photometric dataset of 20 contiguous, medium-band ($FWHM \sim 300$ Å), top-hat filters, that cover the complete optical range $\lambda\lambda$ 3500–9700 Å (see Aparicio Villegas et al. 2010, for further details) over eight non-contiguous regions of the northern hemisphere, amounting to a

[1] http://www.alhambrasurvey.com

total area of 4 deg^2 of the sky (including areas in common with other cosmological surveys such as COSMOS, see Molino et al. 2014, for other overlapping areas). All filters in the optical range have very steep side transmission slopes, close to zero overlap in wavelength, a flat top, and transmissions of 80–95% (Moles et al. 2008). The magnitude limit is $m_{\rm AB} \sim 24$ (5-sigma, measured on 3″) for the 14 filters ranging from 3500 to 7700 Å, decreasing smoothly in the six reddest filters reaching down to $m_{\rm AB} \sim 21.5$ in the reddest one (Molino et al. 2014), which is centred at 9550 Å. The optical coverage is supplemented with the standard NIR J, H, and $K_{\rm s}$ filters, which have a 50% detection efficiency depth (point-like sources, AB magnitudes) of $J \sim 22.4$, $H \sim 21.3$, and $K_{\rm s} \sim 20.0$, analysed in Cristóbal-Hornillos et al. (2009). The ALHAMBRA filter set[2] is designed to optimize the accuracy of photometric redshifts (photo-z, Benítez et al. 2009), but due to their characteristics, it also provides low-resolution photo-spectra composed of 23 bands, corresponding to a resolving power $R \sim 20$ in the optical. All the observations were done under a quality criterion of seeing <1.6″ and airmass <1.8, using the 3.5 m telescope in the Calar Alto Observatory[3] (CAHA) with two cameras, the imager LAICA in the optical range and Omega-2000 for the NIR filters. The actual area for this work is 2.8 deg^2 with a total on-target exposure time of ∼700 h (∼608 h were dedicated for the optical bands, and ∼92 h for the NIR ones) because part of the ALHAMBRA fields have not been imaged yet, although the rest of the fields will be completed reaching the expected total area of 4 deg^2.

The ALHAMBRA Gold catalogue[4] (Molino et al. 2014, hereafter Gold catalogue), is the reference catalogue for this work. As explained in Molino et al. (2014), synthetic $F814W$ images were created, as a linear combination of individual filters, to be used for both detection and completeness purposes, emulating the $F814W$ band of the Advanced Camera for Surveys (ACS) in the *Hubble* Space Telescope (HST). Therefore, the Gold catalogue provides 23 + 1 photometric AB magnitudes (Oke & Gunn 1983) and errors for ∼95 000 bright galaxies ($17 < m_{F814W} < 23$), which are complete up to $m_{F814W} = 23$. Throughout this work, the synthetic $F814W$ photometry is removed from the analysis. Due to the existence of a PSF variability among different filters, the photometry is corrected for PSF and aperture effects. In addition, and for the specific ALHAMBRA case, we quadratically add an extra uncertainty of ∼0.025 (AB magnitudes) in each photometric measurement to account for potential calibration issues or uncertainties.

For further details of the ALHAMBRA survey, we refer readers to Moles et al. (2008) and Molino et al. (2014).

3. The code

Although there are many public codes devoted to carrying out SED fitting in many different ways, e.g. hyperz, STARLIGHT, ULySS, VESPA, Le PHARE, FAST, or SEDfit; we are performing our own analysis techniques to retrieve stellar population parameters from photometric SEDs, specifically designed for analysing the stellar content of galaxies from the ALHAMBRA survey, but being generic and easily adaptable to any multi-photometric survey. Secondarily, there is an increasing number of large-scale multi-filter surveys; e.g. ALHAMBRA, J-PLUS and J-PAS, SHARDS, CLASH, MUSYC, COSMOS, or COMBO-17. They offer a huge amount of photometric data that we can exploit to study the evolution of galaxies, opening a new path to exploring the stellar population of galaxies, overall at intermediate and high redshifts. Although these photometric data are like low-resolution spectra, these techniques present remarkable advantages in comparison with spectroscopy. They can go deeper with a better flux calibration (the calibration of each filter is independent of the rest of them), we can study the stellar content in each resolution element (similar to IFU techniques) with one exposure, and we can work with larger galaxy samples; as a result, it would be a pity not to take advantage of these studies and not exploit all the opportunities that they offer.

The collection of analysis techniques, routines, and other tools that we are using, are collected under the code name MUFFIT, which is written in `Python` language, and it mainly focuses on retrieving the stellar populations of galaxies whose SEDs are dominated by their stellar content.

This section is subdivided in two extended sections. On the one hand, we show in Sect. 3.1 the main ingredients or inputs required to develop the analysis. These preliminary elements are basically composed of the SSP models, the photometric system, and the selection of a dust extinction law to treat the impact of dust on the model SEDs properly. On the other hand, the code is described in Sect. 3.2, emphasizing the description of some specific tasks.

In Fig. 1, we outline the main structure of the code by a brief flowchart that summarises the main features of the followed processes to set constraints on the stellar populations. We caution that the purposes of the flowchart are to help the reader follow the development of Sects. 3.1 and 3.2 and to support the schematic comprehension of the several stages.

The reader who is primarily interested either in the reliability of the code or in the comparison with results retrieved from the literature may skip this section to continue with the self-contained Sects. 4 and 5.

3.1. Main ingredients of the stellar population code

In this section we describe the main input ingredients and preparatory tasks that are considered for developing the stellar population analysis code that is presented in this paper. In particular, our code requires an input set of reference SSP models (Sect. 3.1.1), the photometric system of the data (Sect. 3.1.2), along with a set of recipes to take the intrinsic and Milky Way extinction into account (Sect. 3.1.3). The redshifts of the target galaxy data can be managed as an input ingredient or an output of the code, as explained in Sect. 3.1.4. The flowchart on the left-hand side of Fig. 1 particularly illustrates the main ingredients and preliminary work carried out by the code before starting with the analysis of the data.

3.1.1. The SSP models

The code has been designed to use SSP models as input templates for the comparative analysis of the stellar populations of galaxies. Currently, the code is ready to account for the Bruzual & Charlot (2003, hereafter BC03)[5] and MIUSCAT[6] (Vazdekis et al. 2012; Ricciardelli et al. 2012) SSP models, although any other SSP spectral dataset can be easily implemented.

BC03 is perfectly suited to SED fitting given the large spectral coverage of the models, from 91 Å to 160 μm, allowing us

[2] http://svo2.cab.inta-csic.es/theory/fps3/
[3] www.caha.es
[4] http://cosmo.iaa.es/content/alhambra-gold-catalog
[5] http://bruzual.org/
[6] http://miles.iac.es/

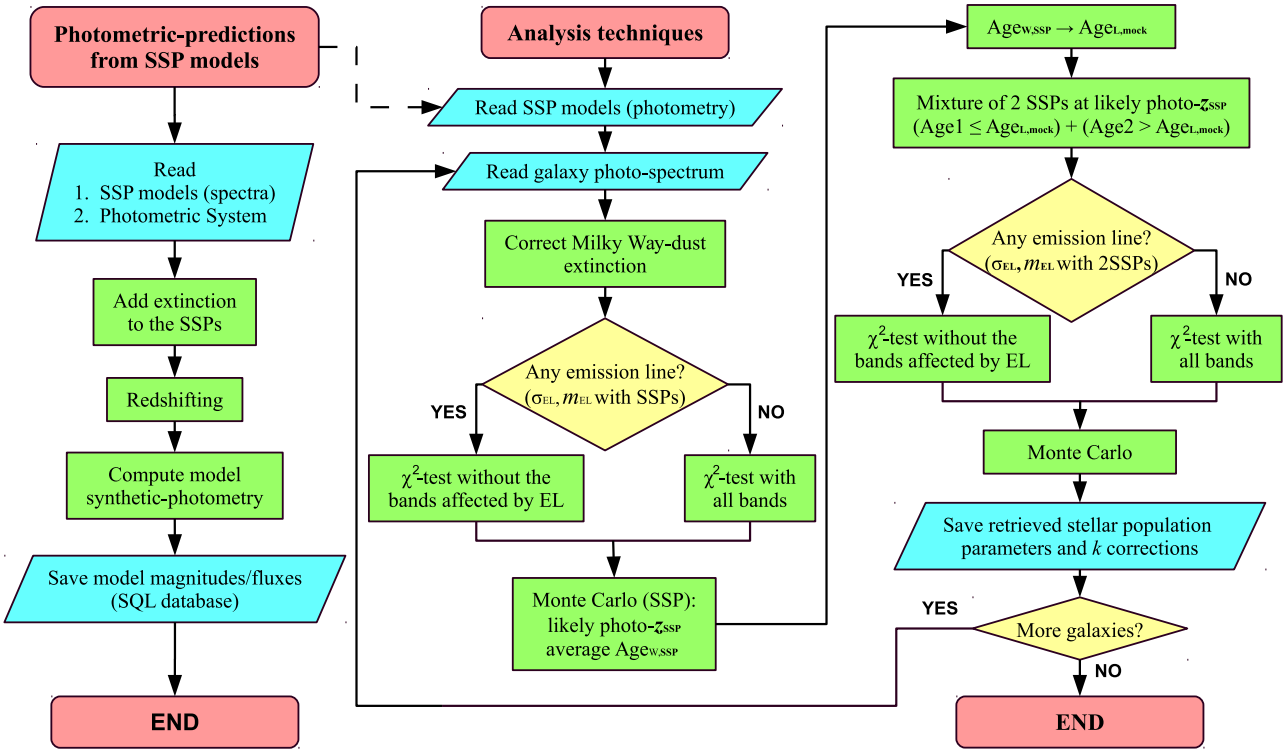

Fig. 1. Flowcharts of the photometric model predictions (*left*) and the analysis techniques (*right*). A more detailed explanation of each step can be found in Sects. 3.1.2, 3.1.3, and 3.2. The dashed row indicates where both processes are related. Flowchart symbols represent standard tasks: ovals, start/end of a process (red); arrows, the direction of logic flow in the process; parallelograms, input/ouput operation (cyan); diamonds, a decision or branch to be made (yellow); and rectangles, a processing step (green).

to cope with most kinds of multi-filter galaxy data, irrespective of the redshift. For the present work, we assume ages up to 14 Gyr and metallicities [Fe/H] = −1.65, −0.64, −0.33, 0.09, and 0.55, Padova 1994 tracks (for further details and references, see Bruzual & Charlot 2003), and a Chabrier (2003) initial mass function (IMF).

MIUSCAT provides a sample of SEDs with a spectral range $\lambda\lambda$ 3465–9469 Å and a resolution of $FWHM \sim 2.5$ Å, almost constant with wavelength (Falcón-Barroso et al. 2011). Despite the great colour calibration of these models, its spectral range is not enough for galaxies at intermediate redshift and further, missing the observed ALHAMBRA colours in the UV range. For this purpose, we extend the lower end of MIUSCAT models up to 1860 Å (A. Vazdekis 2015, priv. comm.), using the Next Generation Spectral Library (NGSL, Heap & Lindler 2007). In addition, we complement these models with their photometric predictions for *J*, *H*, and *K*, which are adapted to predict the ALHAMBRA NIR bands. Throughout this work, we use the models up to 14.13 Gyr with metallicities [Fe/H] = −1.31, −0.71, −0.40, 0.0, and 0.22. We assume a Kroupa Universal-like initial mass function (Kroupa 2001), even though its universality is a current matter of debate (see, e.g. Ferreras et al. 2013). In future works, we will shed light on the systematic variation of the IMF for the more massive galaxies in the ALHAMBRA database.

By construction, the code can also use not only any other set of SSP models, but also any other kind of reference template spectra; for example, as long as their main stellar population parameters (age, metallicity, IMF, extinction, and overabundances), the spectra of real galaxies are assigned by the user. Throughout this paper we do not present this possibility, but concentrate on the performance of the code on the basis of the two SSP model sets mentioned above.

3.1.2. Photometric system and synthetic photometry

For a proper comparison between input SSP models and galaxy data, it is essential to build a reliable estimation of the synthetic magnitudes (or integrated fluxes) of the SSP template models in the same photometric system of the galaxies as the one that needs to be analysed. This is computed by convolving the SSP model or galaxy reference spectra with the response functions of the photometric system. In addition to taking the empirical filter transmission curves into account, in order to obtain a reliable photometric prediction it is advisable to account for specific characteristics of the observing conditions and the instrumental setup employed for the photometric observations of the galaxies to be analysed, for example, the transmittance of the optical system and/or the sky absorption spectrum where the observations were done. The wavelength dependence of the quantum efficiency of charge-coupled devices (CCDs) is remarkable, since typically less sensitive in the bluer and redder ends. If not accounted for properly, this effect modifies the effective wavelength of such filter bandpasses, creating a fictitious colour term in the synthetic photometry of the reference models. Figure 2 presents the response functions of the ALHAMBRA photometric system. It consists of 20 optical bands (left-hand side) and the ALHAMBRA *J*, *H*, and K_s NIR-bands (right-hand side). In this figure, all the effects explained above are already embedded.

We compute the synthetic photometry following the methodology described in Pickles & Depagne (2010), which is based on

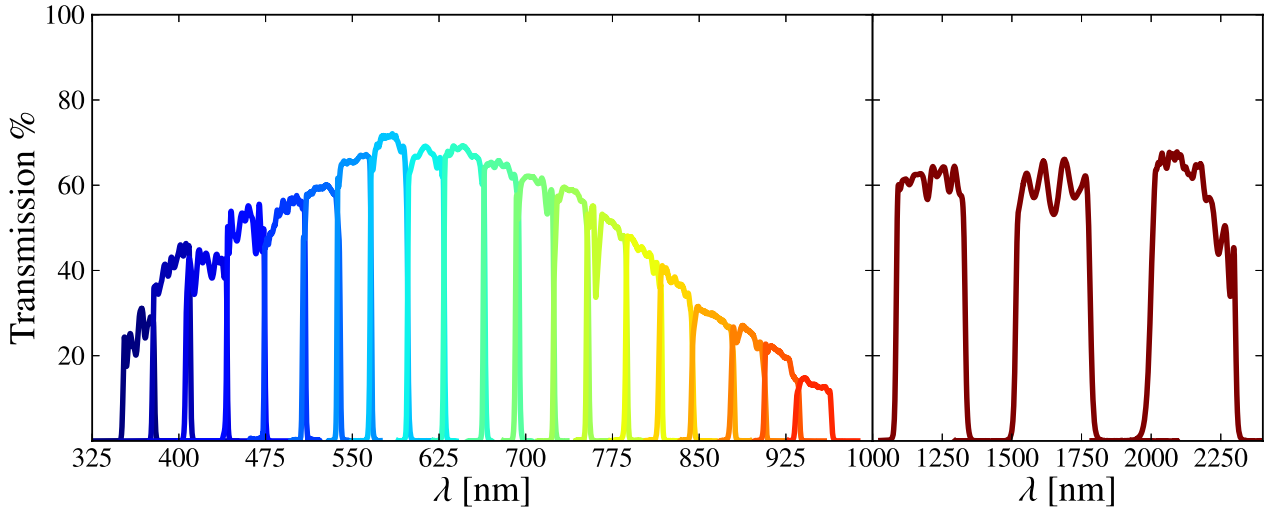

Fig. 2. Response curves of the ALHAMBRA filter set for the CCD 1 in the optical range (LAICA camera; one colour from blue to red per band), together with the ALHAMBRA J, H, and K_s filters (Omega-2000 camera; dark red) to make the model synthetic photometry.

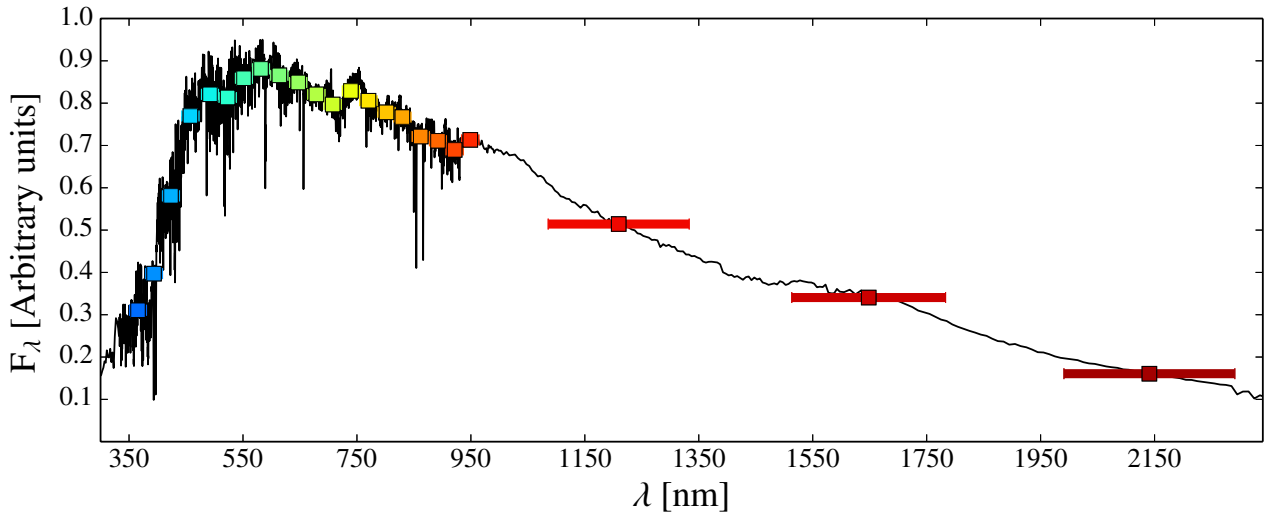

Fig. 3. Synthetic photometry of a SSP using the ALHAMBRA photometric system. The black line is the SSP flux, the colour squares are the expected passbands, and the horizontal bars represent the FWHM of each filter.

the HST `synphot`[7] package and in Bessell (2005). Since current detectors are photon-counting detectors, the number of photons detected across a pass-band X is

$$N_X^{\rm ph} = \int \frac{\lambda}{\rm hc} F_\lambda R_X(\lambda)\, {\rm d}\lambda, \quad (1)$$

where F_λ is the spectrum to convolve, and $R_X(\lambda)$ is the response function of the filter X (also called sensitivity function in some previous work). Normalizing Eq. (1), we get the weighted mean photon flux density,

$$\overline{F_X^{\rm ph}} = \frac{\int \lambda F_\lambda R_X(\lambda)\, {\rm d}\lambda}{\int \lambda R_X(\lambda)\, {\rm d}\lambda}. \quad (2)$$

Some catalogues provide photometry in AB magnitudes, defined as

$$m_{\rm AB} = -2.5 \log_{10} f_\nu - 48.6, \quad (3)$$

where f_ν is the flux in ergs cm^{-2} Hz^{-1} s^{-1}. To transform the weighted mean photon flux density into AB magnitudes, we compute the magnitude of the flux in the STMAG system (system for calibrating HST stars, Stone 1996), which can be easily transformed to the AB magnitude system (Eq. (5)). This intermediate step is necessary because the weighted mean photon flux density is established per unit wavelength, whereas the AB magnitude system is given per unit frequency. The magnitude across the bandpass X in the STMAG system, $m_{{\rm ST},X}$, and in the AB system, $m_{{\rm AB},X}$, is

$$m_{{\rm ST},X} = -2.5 \log_{10} \overline{F_X^{\rm ph}} - 21.1, \quad (4)$$

$$m_{{\rm AB},X} = m_{{\rm ST},X} - 5 \log_{10} \lambda_{\rm pivot} + 18.692, \quad (5)$$

where $\lambda_{\rm pivot}$ is the source-independent pivot wavelength, which is defined as

$$\lambda_{\rm pivot} = \sqrt{\frac{\int \lambda R_X(\lambda)\, {\rm d}\lambda}{\int R_X(\lambda)\, {\rm d}\lambda/\lambda}}. \quad (6)$$

To illustrate this, Fig. 3 shows an example of a SSP spectrum taken from the model set of BC03 (rest frame, solar

[7] http://www.stsci.edu/institute/software_hardware/stsdas/synphot

metallicity, intermediate age of 5 Gyr, Chabrier IMF, and no intrinsic extinction) along with its synthetic photometry using the ALHAMBRA filter set. The spectrum synthetic photometry was computed following the process explained above, where each bandpass is centred at their effective wavelengths ($\lambda_{\rm eff} = \int \lambda R_X(\lambda)\,{\rm d}\lambda / \int R_X(\lambda)\,{\rm d}\lambda$) and the horizontal bars represent the FWHM of each filter. This example is also useful for showing that the main, broader spectral features are easily distinguished after convolving, emphasizing the power of the ALHAMBRA photo-spectra as halfway between classical photometry and spectroscopy.

For the specific case of ALHAMBRA, and because of the configuration of LAICA, we computed four photometric databases for the optical bands, one per CCD, because there are discrepancies among CCD sensitivities and each CCD has its own set of filters. For the NIR-filters J, H, and $K_{\rm s}$, we repeat this process taking the Omega-2000 configuration (only one detector plate). In both optical and NIR synthetic photometry, we take the filter transmission curves into account, the quantum efficiency of every CCD/camera, the sky absorption spectrum at CAHA, and the reflectivity of the 3.5 m-telescope primary mirror with the transmittance of the optical system.

Owing to both the large number of input model parameters (ages, metallicities, extinctions, IMF slopes, and redshifts) and the intermediate-high spectral resolution of current SSP models, it is in general more efficient to build up our set of convolved models once at the beginning, rather than recomputing the model synthetic photometry every time the code is run. After computing the synthetic photometry of all models, the photometric predictions (fluxes and magnitudes), along with the main characteristics of each model, are stored in a structured query language (SQL) database. A straightforward flowchart of the process for estimating photometric predictions is shown on the left-hand side of Fig. 1.

3.1.3. Dust-extinction

Stellar population diagnostic techniques based on SED fitting over a broad spectral coverage, as in this case, require the reddening by extinction to be thoroughly considered to avoid potential misinterpretations of the integrated colours of the population, e. g. older ages or higher metallicities, as well as to derive reliable stellar masses.

Many authors have tried to parametrize the shape of the dust extinction curve (e.g. Prevot et al. 1984; Massa 1987; Mathis 1990; Cardelli et al. 1989; Calzetti et al. 2000; O'Donnell 1994; Fitzpatrick 1999), overall on the bluer parts where the dust reddening is more complex. The dust extinction curve is reproduced well using the parameter $R_V \equiv A_V/E(B-V)$ (Cardelli et al. 1989), which varies between 2.2 and 5.8 depending on the environmental characteristics of the diffuse inter stellar medium (ISM). Although the values of R_V may change depending of the line of sight, throughout this work we assume that the value of this parameter is $R_V = 3.1$, which is the mean value in the diffuse ISM of the MW (Cardelli et al. 1989; Schlafly & Finkbeiner 2011). Amongst the available extinction laws in our code (Prevot et al. 1984; Cardelli et al. 1989; Fitzpatrick 1999; Calzetti et al. 2000), throughout this work we have chosen the Fitzpatrick reddening law (Fitzpatrick 1999) because it reproduces the extinction observed for MW stars well with a preferred mean value around $R_V = 3.1$ (Schlafly & Finkbeiner 2011).

For extragalactic objects, there are two main sources of extinction to account for: on the one hand, the dust intrinsic to the observed galaxy, which is redshifted with the galaxy system; on the other, the foreground dust of the MW, which redden the observed galaxy SED in the observer's reference system. It is important to note that this local MW extinction cannot be corrected with the intrinsic galaxy reddening as the emitted flux is redshifted before being scattered by the dust in our galaxy. As we present below, we separately deal with both extinction effects.

Following a given extinction law, the intrinsic extinction is applied to the SSP template models before they are redshifted and convolved with the photometric system. Throughout this work the values of A_V range from 0.0 to 3.1 (in bins of 0.1 in the range 0.0–1.0, and in bins of 0.3 from 1.0–3.1). The intrinsic extinction can be added as

$$F_\lambda = F_{\lambda,0} \times 10^{-0.4 A_\lambda}, \tag{7}$$

where $F_{\lambda,0}$ is the SSP-model/template flux at rest frame F_λ after adding extinction, and A_λ is determined by the extinction law, which can be chosen by the user. Since it is not clear how R_V varies within a host galaxy and amongst different types of galaxies, we keep the value to $R_V = 3.1$ constant, i. e. the mean value in the MW. This helps to avoid degeneracies and to reduce the number of free parameters, which is already very high and time consuming. Even though the different reddening laws have intrinsic differences (see Fitzpatrick 1999), we do not assume errors in the SSP template models owing to such uncertainties.

We use the dust maps of Schlegel et al. (1998, hereafter SFD), in order to deal with the MW reddening in the line of sight of each galaxy in our sample. The SFD dust maps provide $E(B-V)$ values in different positions of the sky by estimating the dust column density. These estimations were calibrated using galaxies and assuming a standard reddening law to infer the existence of galactic dust between the observer and the sources beyond the MW limits. Since the spatial resolution of SFD is low, $FWHM \sim 6.1'$ and pixel size $(2.372')^2$, MUFFIT makes a bilinear interpolation in the $E(B-V)$ grid for all the galaxy coordinates in the sample.

MUFFIT applies a foreground extinction correction for each individual galaxy photo-spectrum using an extinction law for a value of $E(B-V)$ and R_V. The simplest way to deredden the photo-spectrum of a given galaxy is to compute the extinction in the effective wavelengths of the different filters and then correct the source photometry using the equation

$$F_{\lambda,{\rm c}} = F_{\lambda,{\rm red}} \times 10^{0.4 A_\lambda}, \tag{8}$$

where $F_{\lambda,{\rm c}}$ is the flux corrected for MW extinction for a given wavelength, $F_{\lambda,{\rm red}}$ is the observed flux (reddened), and A_λ the extinction factor given for a extinction law. Since the transmission curves of the filters are not completely flat and the shape of the continuum is source dependent, this approximation may be inappropriate for those filters that exhibit a gradient in their transmission curves (e.g. the lower and upper ends of the ALHAMBRA optical bands, see Fig. 2), especially in the spectral ranges where the observed spectrum is not flat. This effect would be interpreted as a shift in the filter effective wavelength (Fitzpatrick 1999) and, finally, as a colour term in the spectral regions with strong gradients in flux, such as the 4000 Å-break. To get a more reliable correction in this sense, the code carries out the dereddening process of the data in three steps:

– First, we pick up a set of models from BC03 (29 ages, from 0.1 to 10 Gyr, four metallicities, [Fe/H] = −0.64, −0.33, 0.09, and 0.56, and a Chabrier IMF) to be redshifted (redshift bin 0.01) and convolved with the survey photometric system. Before redshifting and computing the synthetic

photometry, we add the intrinsic extinction (A_V from 0.0 to 1.0, in bins of 0.2) to the rest-frame BC03 models. Then, we carry out an error-weighted χ^2 test to find the best fit between the above models and the observed galaxy photometry. The aim of this step is not to derive physical parameters from the best fitting, but to set constraints on the shape of the continuum.
- Second, we re-normalize the BC03 spectroscopic model associated to the best-fitting photo-spectrum. The synthetic photometry of this re-normalized model has to reproduce all the observed photometric bands exactly.
- Finally, we apply Eq. (8) to the re-normalized model derived in the previous step, in order to obtain a dereddened spectrum that we convolve with its related filter response curve. We use the Fitzpatrick (1999) extinction laws to calculate A_λ, the value $E(B-V)$ provided by SFD and $R_V = 3.1$, to deredden all the galaxies of our sample.

In particular, the Fitzpatrick (1999) extinction law was built from the superposition of the extinction curves derived for a set of stars. Consequently, this extinction law contains intrinsic uncertainties, although we would accurately know the values of R_V and $E(B-V)$. We account for the particular uncertainties of this law, adding an error to the dereddened photometry of MW dust, $F_{\lambda,c}$, following the methodology explained in Fitzpatrick (1999) and assuming $\sigma_{R_V} = 0$.

Cosmological fields, often the targets of multi-filter photometric surveys, used to be regions of the sky with low extinction values. In the particular case of ALHAMBRA, our main galaxy sample has MW extinction values of $E(B-V)$ down to 0.04 ($A_V < 0.12$ for $R_V = 3.1$) in all the cases. The colour term due to the MW dust in the ALHAMBRA survey may reach a maximum of $\Delta m_{AB} \sim 0.15$, and the stellar masses may be underestimated by 3% (8%) if we use the K_s (R) filter to estimate it. Although the stellar mass is not primarily affected by MW extinction in these fields, the colour term might change the retrieved stellar populations and consequently the derived stellar mass (see Sect. 3.2.3). In ALHAMBRA there are no galaxies at low Galactic latitudes, $|b| < 5$, where the MW temperature structures are not duly resolved in the SFD maps (Schlegel et al. 1998).

3.1.4. Redshifts

Together with the mass and the stellar population parameters of the galaxy, the code is generically prepared to provide an estimation of the photo-z. It is worth noting, however, that this code is not intended to be a photo-z code. The large number of potential model parameters that the code plays with when the redshift is set as a completely free parameter in the fitting process, means that there is a slight degeneracy with other parameters (like extinction; see Sect. 4.4) that tends to overestimate the derived photo-z. To overcome this effect, the code is also prepared to accept a list of redshift values for each target galaxy as initial constraint: either a list of nominal redshift values, so that the code only performs the fitting process at exactly these redshifts, or complete probability distribution functions (PDF) of redshifts. Then the code only accounts for the model redshifts within the PDF interval. Because of the good results we obtain, we use the photo-z PDFs provided by the ALHAMBRA Gold catalogue as input redshift constraints using BPZ2.0 throughout this work (Molino et al. 2014). It is noteworthy that the combination of our code with the ALHAMBRA photo-z constraints improves the quality of the input photo-z (see Sect. 4.3).

3.2. The core of the MUFFIT analysis techniques

This section is devoted to the main technical features and processes carried out by our code to constrain the stellar population parameters of galaxies in multi-filter data samples. We first describe the way in which the χ^2 minimization is performed in Sect. 3.2.1, with the addition of a mixture of SSPs giving remarkable improvement, which was specifically computed for each galaxy, in order to set more precise constraints on the stellar populations. In Sect. 3.2.2 we explain the process of detecting those bands that may be affected by strong emission lines in detail, helping to understand the overall fitting process. Section 3.2.3 explains how the stellar masses are calculated from the fittings. In addition, a Monte Carlo approach is used to set constraints on the confidence intervals of the parameters provided by the code, detailed in Sect. 3.2.5. Finally, we describe how we manage the k-corrections as a result of the fittings in Sect. 3.2.6. The content of this section is outlined on the right-hand side of the flowchart (see Fig. 1).

3.2.1. The χ^2 minimization and mixture of SSPs

Our stellar population analysis technique is based on error-weighted χ^2 tests between the multi-filter galaxy data and the template SSP models of choice. Since SSP models are usually normalized to a initial stellar mass and both the galaxy distance and its luminosity are uncertain in a general case (in fact these are parameters generally derived from the fit), it is required to add a normalization term, ε, in the classical χ^2 equation. This term minimises the χ^2 value for every model-galaxy pair and it takes all observed bands and associated errors into account, so that the result is only colour dependent. It is more robust for multi-filter surveys because, at most, they only contain a few dozen filters (e.g. 23 in ALHAMBRA). This way, all the meaningful filters contribute to determining the best solution of the fitting (without giving up one of the best bands in order to normalise), and there is no risk that the normalisation band is affected by emission lines or cosmetic defects.

Because the number of reliable bands in each source may be different from one object to the next (for some objects, some filters may be rejected for observational, cosmetic, or calibration problems), in general we divide every χ^2 by the number of available, safe filters in each case. Depending on whether we are working with bandpass fluxes or magnitudes, the χ^2 definition can be expressed as

$$\chi^2_m = \frac{1}{N_p}\sum_{X=1}^{N_p}\left[\frac{O^m_X - (\varepsilon_m + m_X)}{\sigma^m_X}\right]^2, \text{ and} \quad (9)$$

$$\chi^2_f = \frac{1}{N_p}\sum_{X=1}^{N_p}\left[\frac{O^f_X - \varepsilon_f f_X}{\sigma^f_X}\right]^2, \quad (10)$$

where N_p is the number of available filters in an observed galaxy, $O^{m,f}_X$ is the observed X-filter (magnitude or flux), $\sigma^{m,f}_X$ its error, m_X (f_X) the X-filter model prediction (single SSP or SSP mixture, more details below) and ε_m (ε_f) the normalization term. For our purposes, ε_m and ε_f are written as

$$\varepsilon_m = \left(\sum_{X=1}^{N_p}\frac{O^m_X - m_X}{\sigma^{m2}_X}\right)\times\left(\sum_{X=1}^{N_p}\frac{1}{\sigma^{m2}_X}\right)^{-1}, \text{ and} \quad (11)$$

$$\varepsilon_f = \left(\sum_{X=1}^{N_p}\frac{O^f_X f_X}{{\sigma^f_X}^2}\right)\times\left(\sum_{X=1}^{N_p}\frac{f^2_X}{{\sigma^f_X}^2}\right)^{-1}, \quad (12)$$

which correspond respectively to minimizing Eqs. (9) and (10) for each galaxy, i. e., $\partial\chi^2_{\mathrm{m,f}}/\partial\varepsilon_{\mathrm{m,f}} = 0$. As we show later (Sect. 3.2.3), by finding the best stellar population solutions for each galaxy, we can estimate its stellar mass from the ε values.

Equation (9) (the equation used throughout this work) assumes that the distribution of errors is Gaussian, when the distribution of magnitudes is generally not Gaussian since these are logarithmic measurements of flux. From certain signal-to-noise ratios, $S/N \gtrsim 5$ (or uncertainties $\sigma^{\mathrm{m}}_X \lesssim 0.22$), the magnitude uncertainties are quasi-normally distributed, and therefore, this approach is valid. Consequently, we encourage potential MUFFIT users to take fluxes instead of magnitudes when several galaxy bands are compromised by very low signal-to-noise ratios, $S/N \lesssim 4$–5. It must be also taken into account that a certain minimum signal-to-noise ratio is required for determining reliable stellar population parameters without being dominated by degeneracies, as shown later in this paper.

Once we have defined how to compute the fitting goodness, the next step is to compare our set of models to retrieve the most likely stellar population parameters. We carry out this process in two different steps.

- First, we run the χ^2-test described above with the set of SSP models selected by the user (base models), making a first determination of the bands that may be affected by strong emission lines. In short, for each redshift step of the SSP models, the code looks for a flux excess in the galaxy SED with respect to the SSP model SEDs, for all those bands that could be affected by emission lines at the given redshift. A more extensive explanation of our technique of detection of emissions lines in multi-filter galaxy data is presented in Sect. 3.2.2. When this is the case, those bands potentially affected by emission lines are removed from the fitting process, and the χ^2-test is repeated again without the affected bands. In addition, rather than taking the parameters of the best SSP fitting, we carry out a Monte Carlo simulation using the proper signal-to-noise ratios in each filter (further details in Sect. 3.2.5). From the set of parameters retrieved during the Monte Carlo approach, we map the parameter space of compatible solutions (overall age, metallicity, extinction, redshift, stellar mass, and IMF), although at this stage we only focus on the retrieved distributions of age and redshift to carry out the next step: the mixture of two SSPs and its subsequent SED-fitting process.
- Second, according to the age and redshift distributions derived from the initial SSP analysis, we make a new database of models consisting of a mixture of two individual base SSP models. The mixture is only computed for the best redshift solutions determined in the previous step. For each redshift value, the two-model mixture is constrained to combine two SSPs, younger and older than a certain age threshold, $\mathrm{age_T}$, that is related to the most likely age, $\mathrm{age_{SSP}}$, inferred from the Monte Carlo analysis performed in the previous step. This is a reasonable assumption given that the stellar content of galaxies are usually the result of complex SFHs with multiple stellar populations (Ferreras & Silk 2000; Kaviraj et al. 2007; Lonoce et al. 2014), and the age solutions derived from comparisons with single SSPs can be considered to be, in first order, luminosity-weighted means of the ages of the individual, true populations. To determine the $\mathrm{age_T}$ value that allows us to define the limit between younger and older SSP mixtures for each galaxy, we have studied the empirical relation between the luminosity-weighted ages of mock galaxies made of random mixtures of two SSPs, $\mathrm{age_{L,\,mock}}$, and the best age determination for such mock galaxies derived from a single SSP fitting, $\mathrm{age_{SSP}}$. In Fig. 4 we present the result of this study. As expected, we observe that $\mathrm{age_{SSP}}$ underestimates the real age, in particular for $\mathrm{age_{L,\,mock}} \lesssim 6$ Gyr. The yellow curve in Fig. 4 represents $\mathrm{age_T}$ as a function of $\mathrm{age_{SSP}}$. Once the age threshold is established, we generate all the possible SSP combinations (younger and older than $\mathrm{age_T}$), including the stellar mass weight of each component as a new degree of freedom. For a general case with n components per mixture, each magnitude in the band X of the new mixture model is expressed as

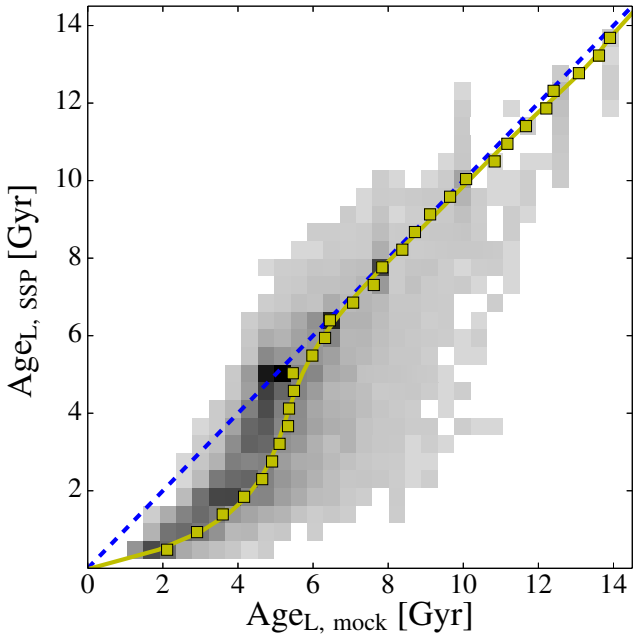

Fig. 4. Empirical relation between the luminosity-weighted ages of mock galaxies made of random mixtures of two SSPs, $\mathrm{Age_{L,\,mock}}$, and the best age determination for such mock galaxies derived from a single SSP fitting, $\mathrm{Age_{SSP}}$. The yellow curve is the $\mathrm{Age_{L,\,mock}}$ median for a given value of $\mathrm{Age_{SSP}}$, and it represents the typical offset in age that one may expect when interpreting the SED of a mixture of two SSPs by fitting a unique SSP.

$$m_{X,\mathrm{mix}} = -2.5\log_{10}\left(\sum_{i=1}^{n}\alpha_i 10^{-0.4\,m^i_X}\right), \quad (13)$$

$$f_{X,\mathrm{mix}} = \sum_{i=1}^{n}\alpha_i f^i_X, \quad (14)$$

where m^i_X (f^i_X) is the magnitude (flux) in the band X for the ith SSP model, and α_i the relative flux contribution of the SSP model in the ith component, with $\sum_{i=1}^{n}\alpha_i = 1$ and $0 \leq \alpha_i \leq 1$. In our case, we are mixing two SSPs and consequently $n = 2$.

After mixing the SSP models as explained above, the code again searches for the best-fitting solution, repeating the detection of emission lines with the mixture of models as explained in Sect. 3.2.2. As in the first step using a single SSP, we not only provide the best solution but also map the compatible stellar-population parameters by a Monte Carlo approach, treating the errors properly in each band. This provides an extra advantage when carrying out a statistical treatment of the results. We devote Sect. 3.2.5 to explaining in

detail how we explore the compatible space of derived parameters for each galaxy.

With this method and two SSPs, one database of mixed SSPs is particularly created for each galaxy, because it is more adequate and realistic than a single SSP fitting. As shown above, for a non-parametric SFH, this represents a substantial improvement over using only one SSP, which is not able to reproduce the colour of an underlying main red population plus less massive and later events of star formation. The mixture of two populations is a reasonable compromise that significantly improves the reliability of determining the stellar population parameters of multi-filter galaxy data (Ferreras & Silk 2000; Kaviraj et al. 2007; Lonoce et al. 2014). In fact, it has been demonstrated (e.g. Rogers et al. 2010) that the mixture of two SSPs turns out to be the most reliable approach to describing the stellar populations of young early-type galaxies, as well as a very reasonable approach for older galaxies where the latter case is only slightly surpassed by the use of chemically enriched exponential models. The two SSP model fitting approach may therefore be generally considered as a reasonable method for analysing the stellar populations of most kinds of galaxies in a consistent way. Moreover, given that MUFFIT does not impose constraints on the metallicities of the two-SSP mixture, this can provide hints not only of age evolution but also of a metallicity build-up. That being said, future versions of MUFFIT will also account for the use of different sets of SSP or τ-models for the best choice of the user.

3.2.2. Emission lines

Nebular emission lines appear frequently in the SEDs of galaxies, even if these are dominated by the light contribution of their stellar content. In particular, dealing with multi-filter galaxy data, filters affected by emission lines may present a substantial excess in flux with respect to any combination of SSP models, because the latter typically do not account for the nebular emission physics. To guarantee the accuracy and reliability of the stellar population parameters derived during the fitting process, it is crucial to detect and remove those bands that can be significantly affected by emission. Not only because they are not comparable to SSP models, but also since filters contaminated by strong emission lines tend to exhibit much higher luminosities and lower photonic errors than the rest of bands, and therefore, these bands would dominate our error-weighted SED-fitting techniques (see Eqs. (9) and (10)). On the other hand, it is worth recalling that the presence of strong emission lines may also provide fruitful information, since they contribute to restricting the feasible redshift intervals of the galaxy. The redshift constraints due to nebular emissions are also considered during the analysis.

The emission line detection process of our code depends on the specific photometric system of the galaxy sample, because it only accounts for those emission lines that are typically strong enough to affect the photometry of the given filter set. It is obvious that the broader the spectral filter width, the larger the equivalent width (EW) of the line that may be potentially detected at a fixed signal-to-noise. In this sense, the code is initially fed with a list of target emission lines that depends particularly on the filter set, customizable by the user, with emission lines, such as [O II] $\lambda\lambda$3726, 3729, [O III] $\lambda\lambda$4959, 5007, H Balmer's series, and [S II] $\lambda\lambda$6717, 6731.

Thanks to the design of MUFFIT, we can also provide a list of typical AGN emission lines to reduce their effects on the fittings, but broad AGN lines may affect two or more ALHAMBRA filters, so the AGN emission line detection criteria in MUFFIT might fail or be inaccurate. It is very important to note that an excessive list of emission lines, mostly when they are spread in the broad wavelength ranges, will eventually derive incorrect results, since too many bands might be removed. It is therefore advisable to restrict this list to the lines that can present a measurable excess in flux, which mainly depends on both the filter widths and the line intensity. For this reason, some bands can be forced by the user to remain in the SED-fitting analysis irrespective of whether they can be potentially affected by emission lines. For instance, in ALHAMBRA we expect that the NIR bands are too wide to be sensitive to the presence of emission lines, so they are never removed during the fitting process even if the code detects a flux excess in any of them.

Once we specify the emission line list in the code, the emission line detection process is carried out in two steps. First, taking the model redshift into account, we fit our models (single SSP or SSP mixture) without all the bands that could be potentially affected by the specified emission lines, and explore the residuals of the best fitting. If the residuals of any of the potentially affected bands present an excess in flux/magnitude greater than a limit value provided by the code user, $\Delta m_{\rm EL}$, and these residuals are deviated beyond a band-error factor, $\sigma_{\rm EL}$, the bands are considered to be affected by emission lines and are removed from the fitting process. Both constraints, $\Delta m_{\rm EL}$ and $\sigma_{\rm EL}$, are required: the latter to assure that the excess in flux is not due to photometric uncertainties, and the former to avoid removing those bands with tiny observational errors that present little discrepancies with respect to the models. Finally, we repeat the fitting without the bands identified in the previous step, getting a new set of reliable χ^2 values, free of nebular contributions.

For the ALHAMBRA case, we use $\Delta m_{\rm EL} = 0.1$, because for lower contributions, the affected bands do not significantly affect the SED-fitting results retrieved with MUFFIT. In addition, we set $\sigma_{\rm EL} = 2.5$ as a reasonable statistical threshold to detect emission lines over the noise. Figure 5 illustrates two SED-fitting examples of two galaxies from ALHAMBRA. The top panel of Fig. 5 illustrates a fitting of a quiescent galaxy in ALHAMBRA without strong nebular emissions, whereas the bottom panel shows a galaxy for which MUFFIT detects that some bands may be affected by emission lines (yellow squares). The red curves represent the observed photo-spectra, while the blue curve is the best-fitting model after the detection of emission lines process. The yellow squares are the bands where the influence of an emission line is ticked, in this particular case Hβ, Hα+[N II], and [S II]. The dashed black lines point out the wavelengths for Hα, Hβ, and [S II] at the galaxy photo-z. For this case, the detection of the emission lines contribute particularly to strongly constraining the redshift range. Despite the ALHAMBRA resolution ($FWHM \sim 300$ Å), we note that strong emission lines can modify the fitting results. In some cases, even Hβ shows significant contributions in the ALHAMBRA dataset.

Since we are providing both those bands that may be affected by strong emission lines and the residuals from the SED fittings, we can easily estimate the flux excesses in order to later transform them to EWs. The advantage of this method is that our best SED-fittings are mixtures of SSPs that already include the corresponding stellar absorptions, so the residuals can be directly related to the absolute nebular emission. The main limitation, in general, comes from the low resolution of the data, because in many cases some filters can be affected by more than one emission line, such as Hα and [N II]. Still, as presented in Sect. 5.2, this technique opens new paths for future work on emission-line galaxies with multi-filter data.

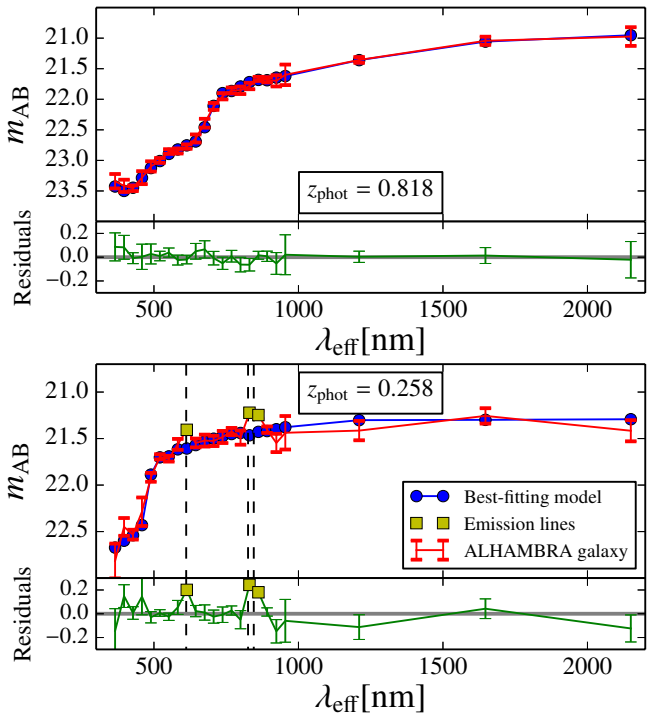

Fig. 5. Spectral fitting examples for galaxies from the ALHAMBRA survey using MUFFIT and the MIUSCAT SSP models. The galaxy photo-spectra and their errors are given in red, whereas the best-fitting models are given in blue. The *top panel* corresponds to a quiescent galaxy for which no emission lines are detected. The *bottom panel* illustrates the case of a star-forming galaxy for which MUFFIT detects three bands affected by emission lines, in yellow. The dashed black lines indicate the wavelengths for Hβ, Hα, and [S II]. Photometric redshifts are given in the insets in the figure.

3.2.3. Stellar masses

As we explain in Sect. 3.2.1, both the normalization term ε introduced in the χ^2 minimization equation and the intrinsic luminosities of the two best-fitted SSPs are directly related to the total stellar mass of the galaxy. SSP models are usually normalized to an initial stellar mass of 1 $M_\odot$, but this decreases with time, thereby accounting for the evolution of the most massive stars. This effect is properly taken into account for determining the final galaxy mass by applying a correction term to each SSP, κ_{SSP}, which is usually provided by the models.

When taking the above considerations into account, the total stellar mass, $M_{\star,T}$, of a mixture of n SSPs (for this work $n = 2$) can be expressed as

$$M_{\star,T} = \sum_{i=1}^{n} M_{\star,\,i} = 10^{-0.4\,\varepsilon_m} \times 4\pi d_L^2 \times \sum_{i=1}^{n} \kappa_{i,\,SSP}\,\alpha_i = \varepsilon_f \times 4\pi d_L^2 \times \sum_{i=1}^{n} \kappa_{i,\,SSP}\,\alpha_i, \quad (15)$$

where $M_{\star,\,i}$ is the stellar mass of each population in the mixture, ε_m is the normalization term defined in Eq. (12), d_L the luminosity distance in cm units (see Hogg 1999), $\kappa_{i,\,SSP}$ the relative stellar mass correction for the ith component in the SSP mixture, and α_i the relative flux contribution of the SSP model in the ith component (see Eqs. (13) and (14)). Throughout this work, the derived stellar masses are quoted including stellar remnants through $\kappa_{i,\,SSP}$, but for a more general case, this parameter may not include remnants.

3.2.4. Stellar population parameters of the SSP mixture

The stellar-population parameters of the mixture of SSPs are estimated from the parameters of each component in the mixture. This can be done in different ways, which mainly depend of the weights assigned to the parameters of the different components. The most common definitions, provided by MUFFIT and employed in this paper, are luminosity-weighted and mass-weighted. The latter provides more realistic information since it accounts for the total mass of stars in each population, hence assigning larger weights to the more abundant or dominant stellar populations. However, these populations may have very different luminosities. In this sense, luminosity-weighted parameters are more representative of the populations that dominate the observed spectrum, since the galaxy SEDs are predominantly led by the brighter populations, even if they are not dominant in relative mass.

Throughout this work, the luminosity-weighted and mass-weighted stellar population parameters of a mixture of n SSPs (for this work $n = 2$), p_L and p_M, respectively, are defined from the stellar population parameters of each ith component (p_i; age, metallicity, extinction, IMF slope, or [α/Fe]) as

$$p_L = \frac{\sum_{i=1}^{n} \alpha_i \times L_i \times p_i}{\sum_{i=1}^{n} \alpha_i \times L_i}, \quad (16)$$

$$p_M = \sum_{i=1}^{n} \frac{M_{\star,\,i}}{M_{\star,T}} p_i = \frac{\sum_{i=1}^{n} \alpha_i \times \kappa_{i,\,SSP} \times p_i}{\sum_{i=1}^{n} \alpha_i \times \kappa_{i,\,SSP}}, \quad (17)$$

where α_i is the relative flux-contribution of the SSP model in the ith component, $\kappa_{i,\,SSP}$ the relative stellar mass correction for the ith component in the SSP mixture, and L_i the luminosity of the SSP model in the observed spectral range. Both definitions agree when the parameter value is the same in each component.

3.2.5. Determining the space of best solutions

Because of the well known degeneracies among stellar population parameters, it is essential to perform a reliable analysis of the possible solutions (as mixtures of two SSPs) for each galaxy according to the uncertainties of the data. For this reason, rather than providing only the best-fitting solution for each galaxy (it is well known that the most likely parameters are not always the best-fitting model parameters), our code accounts for the photometric errors of the multi-filter galaxy data to provide a set of the best-fitting solutions, thereby providing a set of probable values of redshifts, stellar masses, extinctions, and stellar population parameters (ages, metallicities, and IMFs) for each object. These values can ultimately be averaged according to their weights and frequencies to derive the average final parameters assigned to each galaxy and their errors. In this section we explain the processes and the applied criterion used to carry out this analysis.

The determination of the best solution space is based on a Monte Carlo method that, using the proper signal-to-noise ratio of each filter, seeks to find which parameter values are compatible within the photometric errors of the data. Since photometric uncertainties usually follow a normal distribution (or Gaussian), we assume an independent Gaussian distribution in each filter, centred on the band flux/magnitude, with a standard deviation equal to its photometric error. It is worth noting that each filter

is observed and calibrated independently of the remaining ones, so the errors of different filters are not expected to be correlated.

For each galaxy, on the basis of the above Gaussian error distributions for its multi-filter data, MUFFIT generates Monte Carlo simulations (the number of realizations is defined by the user), ending up with a set of multi-filter data realisations for the same galaxy, all of them compatible within the errors. Ideally, the next step would be to run the χ^2 test individually for each realisation of the galaxy using the complete set of models, but this is extremely time-consuming since the code plays with million of models for each fitting (for the present research: 21 ages, 5 metallicities, 18 extinctions, 1 IMFs, 300 redshifts, and solar [α/Fe]). Instead, to speed up this computational process, for each galaxy we perform a preliminary selection of SSP and mixture models that can play an important role in the fitting given the specific SED and errors of the galaxy. This preselection of models is carried out as follows:

i) After having run our code for a certain galaxy SED and having obtained the χ^2 values for all the possible mixture of two SSP models ($\chi^2_{\rm mix}$), we take the $\chi^2_{\rm mix}$ value of the best-fitting model (BFM), $\chi^2_{\rm BFM}$, i.e. the mixture of two SSPs with the greatest probability of being the solution, which corresponds to the lowest $\chi^2_{\rm mix}$ value.
ii) Since the parameter space of best solutions depends not only on the filter photometric uncertainties but also on the shape of the SED, the next step is to determine, for each individual galaxy SED, the range of plausible χ^2 values that are expected according to the set of photometric uncertainties. To do this, MUFFIT performs 10 000 Monte Carlo realisations of the BFM bands according to the Gaussian error distributions of the real galaxy multi-filter data. The corresponding 10 000 χ^2 values between these realisations and the BFM, namely $\chi^2_{\rm M}$, represent the range of χ^2 values that one would expect just due to the photometric uncertainties of the real galaxy data. This range can be very different among different galaxies. In MUFFIT, the limiting plausible value, $\chi^2_{\rm phot}$, is set to the value that encloses the 68.27% (a Gaussian 1σ) of the cumulative distribution function of the $\chi^2_{\rm M}$ values.
iii) Finally, the subsample of possible solutions for a given galaxy SED is composed of those models that fulfil the criterion $\chi^2_{\rm mix} \leq \chi^2_{\rm BFM} + \chi^2_{\rm phot}$. This subsample is consequently restricted to those models whose colours are statistically compatible within the galaxy photon errors.

This way, the set of compatible best solutions for each galaxy is determined by generating $N_{\rm m}$ Monte Carlo realizations of the galaxy SED data (throughout this work $N_{\rm m} = 100$) according to their errors and then running our χ^2 minimization test for each galaxy realisation using the subsample of preselected models as input. In each realisation, we get a new BFM whose parameters are ultimately weighted (ω_j) with its χ^2 value to provide the most likely stellar population parameters together with their errors. Formally,

$$\omega_j = \frac{1/\chi^2_{{\rm MC},j}}{\sum_{j=1}^{N_{\rm m}} 1/\chi^2_{{\rm MC},j}}, \tag{18}$$

$$\langle p \rangle = \sum_{j=1}^{N_{\rm m}} \omega_j p_j, \tag{19}$$

$$\sigma_{\langle p \rangle} = \sqrt{\sum_{j=1}^{N_{\rm m}} \omega_j \left(\langle p \rangle - p_j\right)^2}, \tag{20}$$

where $\langle p \rangle$ and $\sigma_{\langle p \rangle}$ are, respectively, the average stellar population parameters (age, metallicity, extinction, redshift, stellar mass, IMF, and [α/Fe], in a general case) and their errors, and p_j are the stellar population parameters associated to each BFM in the Monte Carlo realisation with a χ^2 value equal to $\chi^2_{\rm MC,j}$. In addition, the essential stellar parameters of each BFM obtained in the $N_{\rm m}$ Monte Carlo iterations are also provided.

Finally, we note that the uncertainties of the parameters retrieved in this stage comprise not only the main parameters of the models, such as ages, metallicities, and IMFs, but also the extinction, the redshift (if it is the case, within the interval provided by an external photo-z code), and the stellar mass.

3.2.6. *K*-corrected luminosities

Once we have computed the best-fitting models, we end up with a combination of SSP models that reproduce the colours of the galaxy photometric SED. As a result, the luminosity of the galaxy, its absolute magnitudes at any band, and the mass-luminosity relation are estimated from exactly the same combination of SSP models taken at rest frame. Independently of the physical parameters linked to the best combination of models, the k-correction is model-independent since it properly reproduces the colours of a galaxy SED at a given cosmological distance, as long as the redshift is well constrained. If we compute the magnitudes for the different bands following this method, the main parameter that determines the k-correction goodness of fitting is the photo-z accuracy. Since the set of SSP models does not contain emission line templates, and our code removes them automatically during the fitting process, the provided k-corrections and luminosities only contain rest-frame predictions about the stellar continuum, not about the nebular content.

To determine rest-frame magnitudes with the corresponding errors, for each galaxy we take all the best-fitting models recovered in the Monte Carlo approach (see Sect. 3.2.5), average them, and provide the average rest-frame magnitudes and their standard deviations, so that we can consider the uncertainties in the photometry thanks to the Monte Carlo approach. It is noteworthy that, at low redshifts, the uncertainties of rest-frame magnitudes may be very high, since the apparent magnitudes depend on the luminosity distance ($\propto d_{\rm L}^{-2}$), which diverges at $z = 0$. This suggests that more accurate photo-z are needed to have better k corrections in the most local Universe. Despite this, the colour terms among different filters are not so affected by this effect, because the major impact is on the source luminosity and not on the rest-frame colours. To minimise this effect, we provide a second k-correction, for which we study the variability of the colours with respect to an anchor band. In short, once we have all the rest-frame models recovered during the Monte Carlo method, the anchor band is the one that presents the lowest variability at rest frame. In ALHAMBRA, this anchor band is usually a band in the red optical part (higher signal-to-noise ratios). This approach turns out to be very useful, for example, for making reliable colour–magnitude diagrams (CMD) at low redshift.

4. Intrinsic uncertainties and degeneracies with ALHAMBRA galaxy data

After having presented the main technical aspects of our SED fitting code in Sect. 3, and before presenting a comparison study between our stellar population results and similar previous data from the literature (see Sect. 5), the goal of this section is to

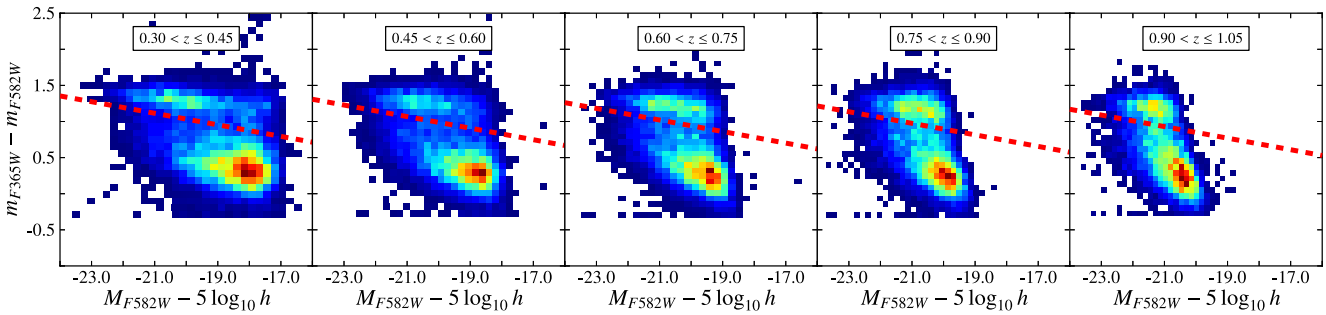

Fig. 6. CMD of the ALHAMBRA galaxies at different redshift bins. The filters *F365W* and *F582W*, both in Vega magnitudes, are used as a proxy for the Johnson filters *U* and *V*. Redder and bluer colours indicate regions of the CMD with higher and lower galaxy densities, respectively. The dashed red line is the colour–magnitude relation that splits the RS from the blue cloud for the mean redshift of the bin, as expressed in Eq. (21).

study the accuracy and reliability of the stellar population parameters retrieved with our code. Since this strongly depends on the photometric system of the data under study, it is important to note that, throughout this section, all the tests and predictions about uncertainties, degeneracies, etc. are performed especially for the ALHAMBRA filter system.

Since the code presented in this paper is particularly suited to studying the stellar populations of galaxies whose SEDs are dominated by their stellar content, we begin to build the CMD of the ALHAMBRA galaxy data in Sect. 4.1, which allows us to properly select our target of galaxies and to compare our results with those published in the literature (Sect. 5). In Sect. 4.2 we check how the intrinsic uncertainties in the photometry of the ALHAMBRA filter system affect the typical errors of the derived parameters, using a set of mock galaxies with well known input parameters. Furthermore, the impact that the uncertainties of the input ALHAMBRA photo-z, Sect. 4.3, have on the derived stellar population parameters is analysed in Sect. 4.4. Finally, we quantify the expected degeneracies among the derived galactic parameters of typical red-sequence galaxies for the ALHAMBRA photometric system and different signal-to-noise ratios.

4.1. Selection criteria of ALHAMBRA red sequence galaxies

It is well known that the CMD of galaxies exhibits a bimodal distribution with two main populations, usually referred to as the "red sequence" (RS) and the "blue cloud" (Bell et al. 2004; Baldry et al. 2004; Faber et al. 2007; Fritz et al. 2014). A large number of RS galaxies are mainly composed of early types (Strateva et al. 2001; Cassata et al. 2007), but since the RS definition is clearly based on the observed galaxy colours, there is also a fraction of star-forming dusty galaxies that may lie on the RS (Williams et al. 2009). To break the degeneracies between quenched galaxies and dusty star-forming galaxies, there are colour-colour diagnostics that use NIR bands (Williams et al. 2009; Arnouts et al. 2013), and even methods that split the CMD into three populations ("red", "blue", and "green") by fitting to a set of SED type classes (Fritz et al. 2014). For the aims of this work, we just follow the classical method of the CMD (Bell et al. 2004; Faber et al. 2007; Fritz et al. 2014). A more detailed study of the contamination of star-forming, reddened galaxies in the RS will be given in a forthcoming paper (Díaz-García et al., in prep.).

To build the sample of RS galaxies, we firstly chose all the galaxies from the Gold catalogue[8] with a statistical STAR/GALAXY discriminator parameter that is lower than or equal to 0.5 (`Stellar_flag` ≤ 0.5) and that is imaged with 70% photometric weight on the detection image (`PercW` ≥ 0.7), to avoid photometric errors in the galaxies close to the image edges. Secondly, we applied our analysis techniques over the full sample of ALHAMBRA galaxies, using the set of MIUSCAT SSP models and the photo-z predictions included in the Gold catalogue, to automatically get their k corrections (see Sect. 3.2.6). From the k corrections and the stellar masses, we can easily estimate their absolute magnitudes, which together with the rest-frame colours, compose the CMD. We note that our CMD does not change significantly if we use another set of models, e.g. BC03, instead of MIUSCAT. In fact, this method is roughly model-independent as we are reproducing the luminosity and colours of the galaxy through the best mixture of two SSP models, irrespective of their parameters, so that the key here is to have a well-constrained photo-z (see Sect. 4.4).

The RS and the blue cloud appear to be clearly separated when the CMD is constructed using the Johnson-like filters *U* and *V* (Johnson & Morgan 1953). In our case, we selected the ALHAMBRA filters *F365W* and *F582W* for simplicity, because these are the ones whose effective wavelengths are like *U* and *V*, respectively. The CMD of the ALHAMBRA galaxies based on the *F365W* and *F582W* filters is presented in Fig. 6, where redder colours indicate higher and bluer colours and lower galaxy densities, respectively. Following the equation provided in Bell et al. (2004), which is compatible with the relation obtained in Fritz et al. (2014), we define the RS as those galaxies redder than the following colour–magnitude relation:

$$m_{F365W} - m_{F582W} = 1.15 - 0.3z - 0.08(M_{F582W} - 5\log h + 20), \quad (21)$$

where m and M indicate apparent and absolute magnitudes in the Vega system. By simple visual inspection, it is clear that Eq. (21), illustrated in Fig. 6, splits the RS from the blue cloud properly, which already constitutes a first-order check of the goodness of the SED fitting.

4.2. Photon-noise uncertainties

To analyse the intrinsic uncertainties in the derived stellar population parameters of the galaxies due to the photon-noise errors of the ALHAMBRA photometry, we created mock galaxies consisting of a mixture of two random SSPs, in which we add photon noise according to the sensitivity of the ALHAMBRA filters and to the SED of the mock galaxies. By construction, this test is fairly representative of the performance of RS galaxies. After adding noise, we ran our code in order to derive the stellar

[8] http://cosmo.iaa.es/content/alhambra-gold-catalog

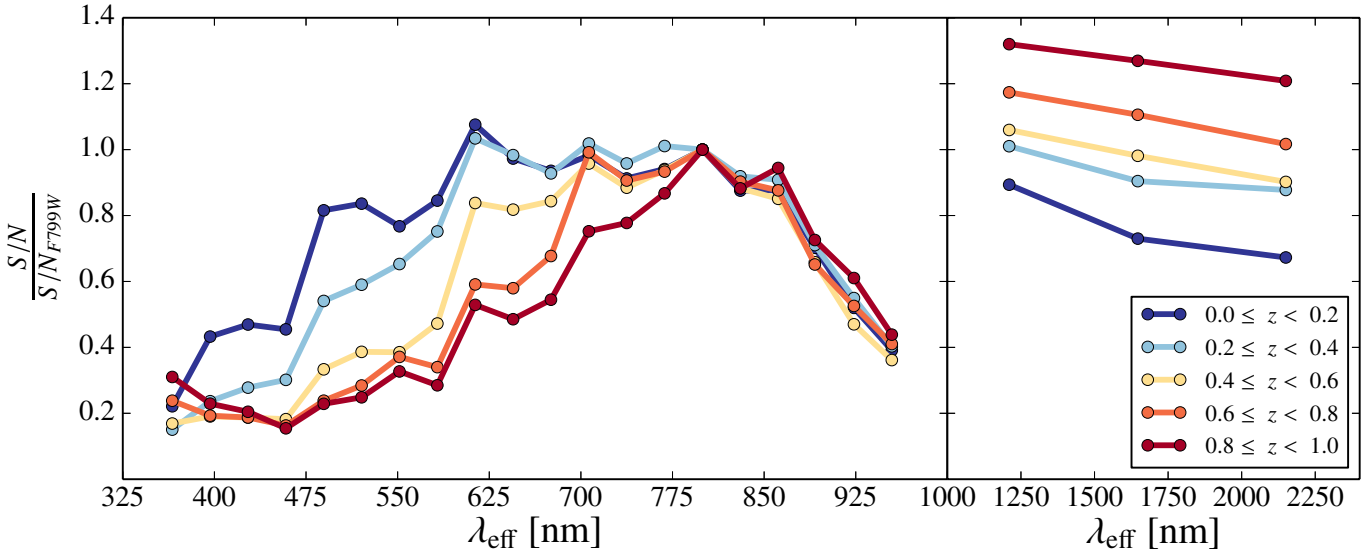

Fig. 7. Typical signal-to-noise ratios per filter for real ALHAMBRA red sequence galaxies in different redshift bins. The signal-to-noise ratios are normalized to that of the *F*799*W* filter. The observed data points account for the effective throughput of the telescope plus camera system and for the average SEDs of red sequence galaxies.

population parameters of these mock galaxies, treating them as observed galaxies, but as ones for which we know the real values of their parameters. The comparison between the input and the output parameters, as a function of the signal-to-noise ratio of the filters, allows us to conclude something about the main topic of this section.

We took the extended version of the MIUSCAT models (see Sect. 3.1.1) with the Kroupa IMF to develop these simulations. After adding different extinction values (Fitzpatrick's law, A_V values ranging from 0.0 to 0.8 in steps of 0.1) at different redshifts (from 0 to 1 and a step of 0.01), we randomly mixed two SSPs with a series of constraints:

- The weight of the younger population should not be more than 30% in mass, and its age not be larger than 4 Gyr. The mass limit is required to avoid luminosity-weighted ages that are too low, which is unlikely in RS galaxies (Kaviraj et al. 2007), and to guarantee the presence of old galaxies at all redshifts.
- The age of the random SSPs cannot be much older than the age of the Universe at that redshift. Since the ages of SSP models are a discrete set of values, we state the limit to the first model that surpasses the age of the Universe at each redshift.
- The extinction of both SSPs is the same. Although this may not necessarily be the case in general, it is a reasonable assumption because we are studying integrated stellar populations, which translates to an average intrinsic extinction that affects the projected incoming light from different populations.

To properly sample the galaxy mass range, we assigned random stellar masses in the range $9.5 \leq \log_{10}(M_\star/M_\odot) \leq 12.5$. We repeated this process 2 000 times per interval of redshift from 0 to 1 in bins of 0.2, getting 10 000 mock galaxies. As we explain below, we study the impact of the signal-to-noise ratio for three cases (S/N = 10, 20, and 50). In each case, we constructed a new random sample of mock galaxies, with the total number of simulations 30 000.

After having built the set of toy mock galaxies, it is important to accurately model the way the galaxies are seen by the ALHAMBRA photometric system. It is at this point where the ALHAMBRA configuration plays an important role. The ALHAMBRA characteristics (see Fig. 2 and Sect. 3.1.2) are such that the reddest bands are not as deep as the rest of the LAICA filters. On the other hand, the SED of typical RS galaxies, even the youngest ones, exhibit a clear flux drop in the blue region, with a prominent 4000 Å-break in the middle. Therefore, we cannot assume either that all the filters present the same signal-to-noise ratio or that the signal-to-noise ratio among filters does not depend on the redshift.

To carry out a realistic simulation, we take all the galaxies from the ALHAMBRA Gold catalogue for which the best-fitting corresponds to a RS galaxy (see Sect. 4.1), and compute, for every galaxy, the signal-to-noise ratios in each filter relative to the *F*799*W* filter, which is on average the band with the maximum signal-to-noise ratio at any redshift. By repeating this process in different redshift bins, we determine how the signal-to-noise ratio changes along the SED as a function of the signal-to-noise in the anchor band *F*799*W*. These curves are shown in Fig. 7, and they account for the effective throughput of the telescope plus camera system, and for the average SEDs of RS galaxies. The signal-to-noise ratios of the reddest filters up to $z = 1$ are strongly affected by technical features of the survey (mainly the depth in these bands), whereas the bluest filters are also affected by the SED shape. From the curves in this figure, it is easy to see how the 4000 Å break moves from blue to red wavelengths when the redshift increases. Interestingly, at higher redshifts, the signal-to-noise ratio of the bluest filters starts to grow, indicating larger fluxes in these bands, probably due to the presence of young populations in the galaxy (Ferreras & Silk 2000), which are easily observable at higher redshifts. Regarding the NIR filters, we checked that typical RS galaxies become redder, on average, when they are observed at higher redshifts.

To study the impact of different signal-to-noise ratios on the derived stellar population parameters, we added noise to the mock galaxies, in each case taking the suitable signal-to-noise ratio curve depending on its redshift. We built three samples of 10 000 mock galaxies, and in each sample we forced the mean signal-to-noise ratio per mock photo spectrum to be S/N = 10, 20, and 50, respectively; that is, for a galaxy with

Table 1. Typical uncertainties in the determination of redshifts, extinctions, luminosity-weighted ages, luminosity-weighted metallicities, and stellar masses, expected from running our code on ALHAMBRA red sequence galaxies at different redshift bins and for different S/N (10, 20, and 50).

Parameters	$0.0 \le z \le 0.2$	$0.2 \le z \le 0.4$	$0.4 \le z \le 0.6$	$0.6 \le z \le 0.8$	$0.8 \le z \le 1.0$
$S/N = 10$					
$z_{\rm phot}$	0.01 ± 0.03	0.00 ± 0.04	0.00 ± 0.03	0.00 ± 0.02	0.00 ± 0.02
A_V	0.10 ± 0.22	0.08 ± 0.20	0.04 ± 0.17	0.04 ± 0.15	0.02 ± 0.14
$\log_{10}$ Age$_{\rm L}$ [yr]	-0.01 ± 0.19	-0.03 ± 0.17	-0.03 ± 0.14	0.00 ± 0.11	0.03 ± 0.10
$[{\rm Fe/H}]_{\rm L}$	-0.09 ± 0.29	0.01 ± 0.30	0.03 ± 0.26	0.00 ± 0.23	0.03 ± 0.22
$\log_{10} M_\star\ [M_\odot]$	0.10 ± 0.28	0.02 ± 0.12	0.01 ± 0.10	0.01 ± 0.08	-0.01 ± 0.06
$S/N = 20$					
$z_{\rm phot}$	0.00 ± 0.01	0.00 ± 0.01	0.00 ± 0.01	0.00 ± 0.01	0.00 ± 0.01
A_V	0.06 ± 0.15	0.04 ± 0.13	0.01 ± 0.10	0.02 ± 0.09	0.00 ± 0.08
$\log_{10}$ Age$_{\rm L}$ [yr]	-0.03 ± 0.14	-0.03 ± 0.13	-0.01 ± 0.11	0.00 ± 0.09	0.01 ± 0.07
$[{\rm Fe/H}]_{\rm L}$	-0.06 ± 0.20	-0.03 ± 0.19	-0.01 ± 0.16	-0.01 ± 0.14	0.00 ± 0.12
$\log_{10} M_\star\ [M_\odot]$	0.02 ± 0.15	0.01 ± 0.09	0.00 ± 0.07	0.00 ± 0.06	-0.01 ± 0.05
$S/N = 50$					
$z_{\rm phot}$	0.00 ± 0.00	0.00 ± 0.00	0.00 ± 0.00	0.00 ± 0.00	0.00 ± 0.00
A_V	0.01 ± 0.08	0.00 ± 0.06	0.00 ± 0.05	0.00 ± 0.03	0.00 ± 0.02
$\log_{10}$ Age$_{\rm L}$ [yr]	-0.02 ± 0.11	-0.02 ± 0.09	0.00 ± 0.08	0.00 ± 0.06	0.00 ± 0.05
$[{\rm Fe/H}]_{\rm L}$	-0.03 ± 0.08	-0.02 ± 0.08	-0.02 ± 0.07	-0.02 ± 0.06	-0.01 ± 0.05
$\log_{10} M_\star\ [M_\odot]$	0.00 ± 0.08	0.01 ± 0.06	0.00 ± 0.05	0.00 ± 0.04	0.00 ± 0.03

Notes. The random errors in the parameters are given as the mean and rms of the best Gaussian function that reproduces the distribution of the differences between the input and output parameter values, as illustrated in the right panels of Fig. 8.

$S/N = 20$ at redshift 0.5, the mean signal-to-noise for the 23 filters is 20, but in the bluest filter $S/N_{F365W} \sim 6$, and in the anchor band (maximum) $S/N_{F799W} \sim 30$. The values of $S/N = 10$, 20, and 50 correspond to median apparent magnitudes for the detection band of $m_{F814W} \sim 22.6$, 21.4, and 19.8, respectively (ALHAMBRA RS galaxies and AB magnitudes). For the anchor band $F799W$, these values are almost identical. In ALHAMBRA, typical errors in the zero points due to calibration issues are ∼0.025 (AB magnitudes), which correspond to a signal-to-noise ratio of ∼50. Furthermore, most (≳80%) of our ALHAMBRA RS subsample has a mean signal-to-noise ratio over 10, whereby these values ($S/N = 10$, 20, and 50) are suitable for our simulations.

Although for the mock galaxies we take models with $0.0 \le A_V \le 0.8$ and $0.0 \le z \le 1.0$, for the mock analysis we use SSP models with redshifts up to 1.2 and extinctions up to 1.0 to avoid border effects in the parameter estimation. Concerning the age estimation, we use the same constraint as in the mocks; i.e., depending on the redshift, the oldest ages are not allowed.

Figure 8 illustrates the comparison between the input parameters of the mock galaxies and the output parameters retrieved with MUFFIT, for the case $S/N = 20$ and all redshifts. The left-hand panels present one-to-one comparisons for the input and output photometric redshifts, extinctions, luminosity-weighted ages and metallicities, and stellar masses. Right-hand panels illustrate the distributions of the differences between the input and output values in each case, fitted to a Gaussian function (in red) whose mean and rms are therein indicated. In addition, Table 1 provides the typical mean differences and their rms for different redshift bins and $S/N = 10$, 20, and 50.

As expected, overall there is a very good agreement between the input stellar-population parameters of the mock galaxies and the ones provided by MUFFIT after applying the correspond noise curve on the preceding mock galaxies. This is not surprising since we are analysing mock galaxies made of mixtures of two SSP models, with the same SSP models as input for our code. In this sense, this test must be considered as a lower limit to the parameter uncertainties that we can expect for the forthcoming analysis of ALHAMBRA galaxies, only because of the photon-noise photometric errors. As a matter of fact, the total errors in the derived parameters are expected to be larger, owing to potential differences between the spectro-photometric systems of the ALHAMBRA data and the models, independently of the SSP models of choice. In addition, real galaxies may be affected by ISM emissions or AGNs, which modify their SEDs with respect to a classical mixture of SSPs.

Looking at the stellar mass plot in Fig. 8, there seems to be a slight overestimation of the stellar mass. These cases correspond to galaxies with $z \lesssim 0.02$, for which small variations in the redshift cause big changes in the luminosity distance, hence in the retrieved stellar mass (see Eq. (15)). This result suggests that in the very local Universe, more accurate redshifts are required to provide reliable stellar masses using the analysis techniques explained above. Fortunately, the very few local galaxies in the ALHAMBRA survey have a very high signal-to-noise ratio as well, so that this overestimation is negligible in our case.

Another case that is worth being explained is the one of mock galaxies with low extinctions and low metallicities. According to Fig. 8, we are getting higher values on average. However, this is an artefact of the simulations since there are no lower values in our set of SSP models. The important result in these plots is that we are still retrieving the right trend in the parameters, despite the border effects in the parameter space.

The results in Table 1 are divided into different redshift bins because old ages are not allowed at high redshifts. It is noteworthy that all the parameters are determined better at high redshifts than at low redshifts at the same mean signal-to-noise ratio. First, because at higher redshifts the galaxy SEDs are sampled with an

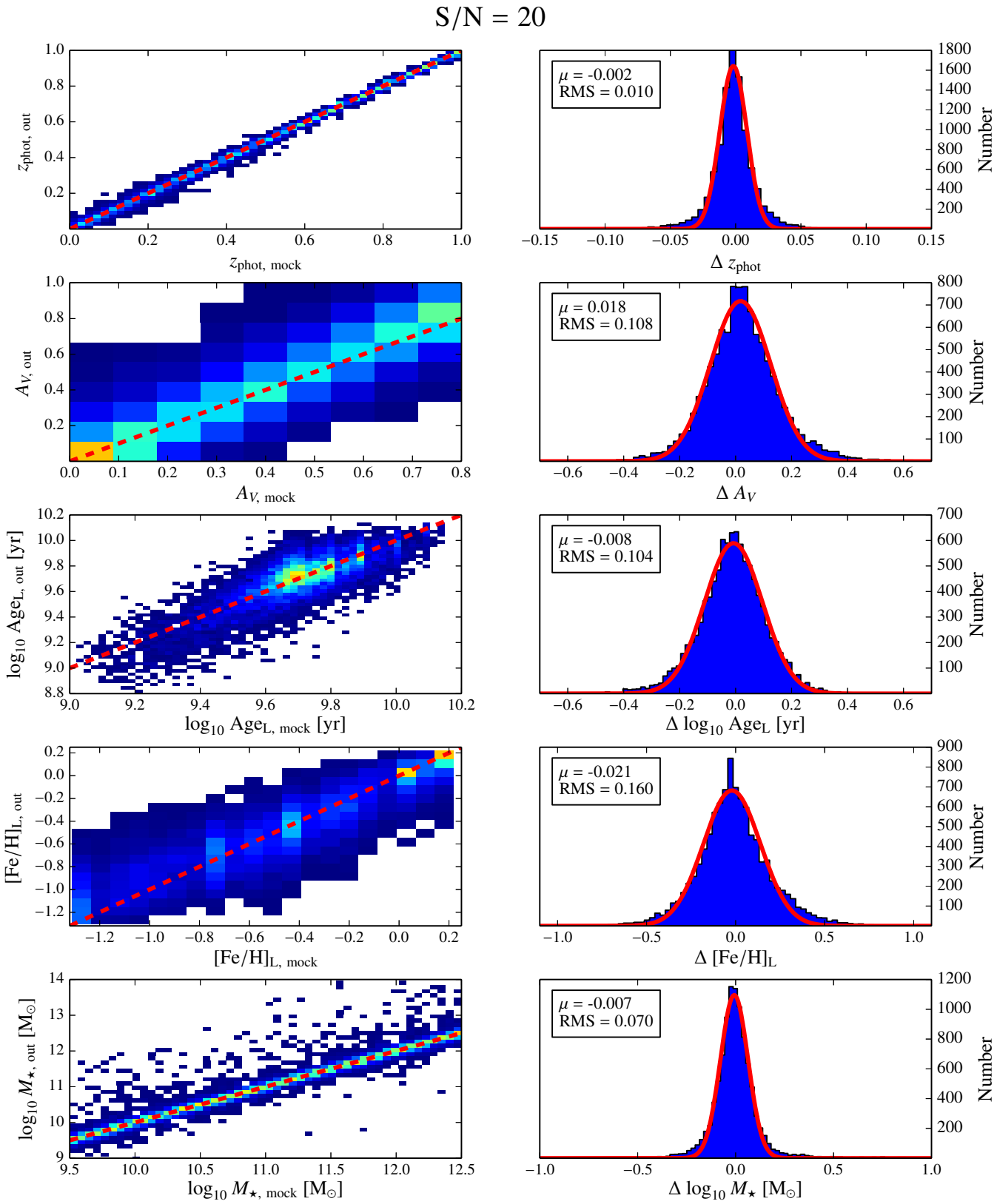

Fig. 8. Comparison between the input parameters of mock ALHAMBRA galaxies, consisting of random mixtures of two SSP models, and the output parameters retrieved with MUFFIT. The mock galaxies (RS-like galaxies) have average signal-to-noise ratios per filter of 20, according to the typical signal-to-noise ratio distribution presented in Fig. 7. *Left panels* show, *from top to bottom*, the one-to-one comparisons in redshift, extinction, luminosity-weighted age, luminosity-weighted metallicity, and stellar mass. Redder and bluer colours indicate regions with higher and lower solution densities, respectively. The red dashed line indicates the one-to-one relationship. *Right panels* present the distributions of the differences between the input and output values in each case, fitted to a Gaussian function (in red) whose mean and rms are indicated within the box.

equivalent higher spectral resolution at rest frame, so that both redshift and age, which are sensitive to the 4000 Å break, are better established (and consequently, the rest of parameters as well). Also, at high redshift the range of possible ages is shorter, and are in turn younger with lower degeneracies than their older counterparts. Finally, the bluest parts of the $z \gtrsim 0.5$ SEDs have higher signal-to-noise ratios. These filters act as anchoring bands to constrain blue-sensitive parameters (like extinction or metallicity). This growth in the signal may be due to an underlying young and less massive population in the galaxy (Ferreras & Silk 2000) that is not strong enough to contribute in the optical range, but that dominates the flux in the NUV rest-frame regime (being visible at $z \gtrsim 0.5$ in ALHAMBRA), reinforcing the necessity of using two components in the fittings.

To conclude, these simulations are key for giving us an idea of the typical issues that may appear in this kind of study and the uncertainties that we expect from photon-noise photometric uncertainties. These results show that one can robustly explore the stellar populations of galaxies in the ALHAMBRA dataset by using the MUFFIT code presented here.

4.3. Photometric redshifts in the ALHAMBRA survey

Although the main aim of our code is not to determine redshifts, it is very important to check whether, for a general case in which the galaxies do not have any redshift information, the code is self-sufficient for estimating photo-z properly, at least to some extent. Otherwise, the derived galaxy parameters may be estimated incorrectly.

To do this, we ran our code on the subsample of RS galaxies with spectroscopic redshifts in ALHAMBRA, from Molino et al. (2014), to set the accuracy of the ALHAMBRA photo-z. This subsample is built by the publicly available data of the spectroscopic surveys that overlap with ALHAMBRA (zCOSMOS, Lilly et al. 2009; GROTH, Davis et al. 2007; and GOODS-N, Cooper et al. 2011), amounting to ~900 RS galaxies up to magnitude $m_{F814W} < 22.5$. For the purpose of this test, we used the photo-z predictions provided by BPZ2.0 in the Gold catalogue. In addition, we also took the photo-z constraints provided by EAZY (Brammer et al. 2008) with the default configurations and templates, to assess whether MUFFIT also works similarly when the input photometric redshifts come from an external source.

To provide a numerical value for the quality and accuracy of the photo-z, we simultaneously use definitions, which can be more or less useful depending on our purposes for both accuracy and catastrophic outliers. Brammer et al. (2008) propose the normalized median absolute deviation, $\sigma_{\rm NMAD}$, as a measurement of the photo-z uncertainties, since it estimates the deviation of the photo-z distribution without being affected by catastrophic errors. It is defined as

$$\sigma_{\rm NMAD} = 1.48 \times \text{median}\left(\frac{|\Delta z - \text{median}(\Delta z)|}{1 + z_{\rm spec}}\right), \quad (22)$$

where $\Delta z = z_{\rm phot} - z_{\rm spec}$. Furthermore, we provide the rms of the distribution $\Delta z/(1 + z_{\rm spec})$, which in the following, we denote as $\sigma_z/(1 + z_{\rm spec})$. Additionally, we use two definitions for the rate of photo-z catastrophic outliers, as in Molino et al. (2014), formally expressed as

$$\eta_1 = \frac{\Delta z}{1 + z_{\rm spec}} > 0.2, \text{ and} \quad (23)$$

$$\eta_2 = \frac{\Delta z}{1 + z_{\rm spec}} > 5 \times \sigma_{\rm NMAD}. \quad (24)$$

Table 2. Quality of the photo-z retrieved for a subsample of RS galaxies in ALHAMBRA, when different method are applied: our code alone, BPZ2.0, EAZY, and our code using BPZ2.0 and EAZY as input values of redshift.

	$\sigma_{\rm NMAD}$	$\sigma_z/(1+z_{\rm s})$	η_1	η_2
MUFFIT	0.0157	0.0105	1.6%	5.8%
BPZ2.0	0.0104	0.0076	0.9%	7.7%
EAZY	0.0102	0.0083	0.8%	4.0%
MUFFIT + BPZ2.0	0.0087	0.0070	0.9%	6.3%
MUFFIT + EAZY	0.0092	0.0071	0.7%	5.5%

Notes. Details on the definition of the quality values are given in Eqs. (22)–(24).

On the basis of the above equations, Table 2 presents the quality of the photo-z determined for the subsample of RS galaxies with different methods. First, we analysed the reliability and accuracy of the photo z derived from our own code alone, that is, not using any photo-z value as input to constrain the solution. This case can be directly compared with the values directly derived from the BPZ2.0 and EAZY codes, showing, as expected, that photo-z codes do a better job of determining redshifts from scratch. In addition, we analysed the quality of the photo z derived in the same way from our code when the redshift PDFs of BPZ2.0 are used as input parameters. MUFFIT explores the plausible stellar population parameters, managing the photo z as another free parameter inside the redshift range of choice for the user. For the present work, we used the 1σ PDF range provided in the Gold catalogue, hence all the photo-z weights equal to 1 inside the provided range $(1 - \sigma)$ and 0 beyond this range. According to Eqs. (22)–(24), we obtained $\sigma_{\rm NMAD} \sim 0.0087$, yielding a rate of catastrophic outliers $\eta_1 = 0.97\%$ and $\eta_2 = 6.26\%$. For this specific case, the resulting photo z were compared with their spectroscopic counterparts in Fig. 9. Similarly, using the photo-z constrains from EAZY as an input to our code (also $1 - \sigma$, for consistency in the comparison), we find $\sigma_{\rm NMAD} = 0.0092$, $\eta_1 = 0.76\%$, and $\eta_2 = 5.51\%$. From these results we conclude that, at least for RS galaxies, our stellar population code improves the redshift accuracy of classical photo-z codes, when these are used as input for our technique. This can be explained as our method plays with mixtures of much larger numbers (million) of SSP models, allowing flexible SED fittings to be performed, hence providing a fine-tuned, second-order correction to the redshift values of photo-z codes. In addition, the number of catastrophic outliers, η_1 and η_2, is also marginally decreased on average. The shifts between photo-z and spectroscopic values are statistically insignificant ($\lesssim$0.002), as we see in Sect. 4.4, on our stellar population results. As we show in Sect. 4.4, devoted to setting constraints on the uncertainties of the stellar population parameters due to the photo-z uncertainties, it is more important for our aims for the stellar population to minimise the number of outliers, rather than decreasing $\sigma_{\rm NMAD}$ a little.

4.4. Impact of the photometric-redshift uncertainties

One of the most critical parameters for determining reliable stellar populations and masses for a galaxy is the redshift. If the redshift is unknown or uncertain, it is obvious that the rest of the derived parameters will not be reliable either. In this section, we aim to quantify the impact of the typical redshift uncertainties on the reliability of the retrieved parameters and the maximum redshift errors allowed to reach our goals.

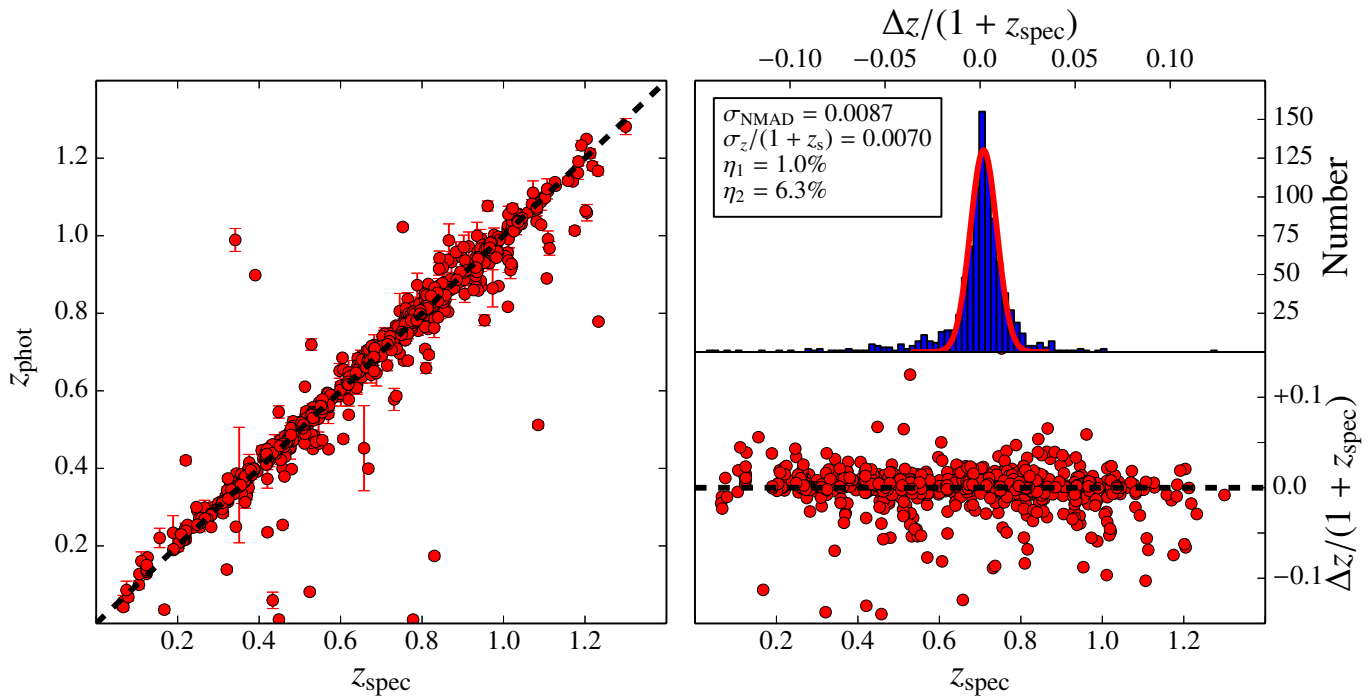

Fig. 9. Comparison of the photo-z retrieved with our code using the redshift PDFs of BPZ2.0 as input values. The data correspond to a sub-sample of RS galaxies from ALHAMBRA with spectroscopic redshifts in the literature. *Left panel* illustrates the one-to-one redshift comparison for every galaxy, with the dashed line being the one-to-one relation. The *bottom-right panel* presents the differences between the photo-z and their spectroscopic counterparts for each galaxy, normalized by $(1+z_{\rm spec})$. The *top-right panel* shows the obtained distribution $\Delta z/(1+z_{\rm spec})$, indicating the accuracy parameters and the rate of outliers (Eqs. (22)–(24)) at the inner box.

To answer these questions, we again focus on the ALHAMBRA data. To determine the direct impact of redshift uncertainties over the rest of derived parameters, we compared the results obtained from our code for the spectroscopic sub-sample of RS galaxies (see Sect. 4.3) using the redshift PDFs of BPZ2.0 as input, with the results that we obtained with our code for the same galaxy sample assuming exactly their spectroscopic redshifts. It is worth noting that, in contrast to the previous simulations (e.g. Sect. 4.2), we were using real galaxies to estimate these uncertainties.

Figure 10 summarises the results of this test. Left-hand panels present the one-to-one comparison for the redshift, extinction, luminosity-weighted age, luminosity-weighted metallicity, and stellar mass. To facilitate the visual interpretation of the comparison and observe the direct effect of the worst estimated photo-z on the stellar population parameters, we plot each galaxy with a colour depending on the discrepancy level of its photo-z using the above definitions of catastrophic outliers (η_1 and η_2, see Eqs. (23) and (24)). This is clearly seen in the top left-hand panel of Fig. 10, where the redshift values are compared. From the data in Fig. 10 and the rms of the differences, we observe that, overall, the stellar population parameters present very minor changes due to typical redshift uncertainties and all the distributions are centred close to zero. On average, such uncertainties account for $\sigma^z_{A_V} = 0.03$, $\sigma^z_{\rm Age} = 0.18$ Gyr (0.03 dex), $\sigma^z_{\rm [Fe/H]} = 0.04$ dex, and $\sigma^z_{M_\star} = 0.03$ dex, which are all negligible when we compare them with the uncertainties introduced by the typical photon noise (see Sect. 4.2). As expected, catastrophic outliers ($|z_{\rm phot} - z_{\rm spec}| \geq 0.044$) exhibit a larger spread in most parameters.

To conclude, the typical uncertainties on the redshifts present a negligible impact on the main stellar population parameters, except if the galaxy is a catastrophic outlier. The uncertainties on the ALHAMBRA photometry and the model systematics are more crucial uncertainties in the present work.

4.5. Degeneracies

In addition to estimating the uncertainties, it is crucial to know which kind of degeneracy may alter our results, to avoid unveiling a finding that really is a degeneracy aftermath. To interpret the output properly, we must keep these degeneracies under control, reducing their impact as much as possible.

Unlike stellar population diagnostic techniques based on local absorption features, such as classical line strength indices, which also present the well known age-metallicity degeneracy (Worthey 1994), our multi-filter stellar population code depends on colour, because it tries to reproduce the galaxy SED by mixing SSPs over a wide wavelength range. Therefore, considering only the age-metallicity degeneracy may not be enough, since we must evaluate any parameter that can modify the colour in a wide wavelength range; that is, we also have to include the intrinsic extinction as another degenerated parameter in our analysis. As we mention above, in this paper we assume a universal IMF. Otherwise, this parameter should be considered for the degeneracies as well, as bottom-heavy IMFs exhibit redder colours than top-heavy ones. Moreover, since the degeneracies amongst parameters strongly depend on the number and width of the filters, the total spectral coverage, etc., it is worth noting that the results presented in this section only apply to the use of our code on ALHAMBRA data.

To address the degeneracy questions in the most realistic way, we take all the ALHAMBRA RS galaxies as targets (see Sect. 4.1) with mean signal-to-noise ratios of ∼20 and in certain ranges of age and metallicity. These results come up after having run MUFFIT with the ALHAMBRA galaxies using

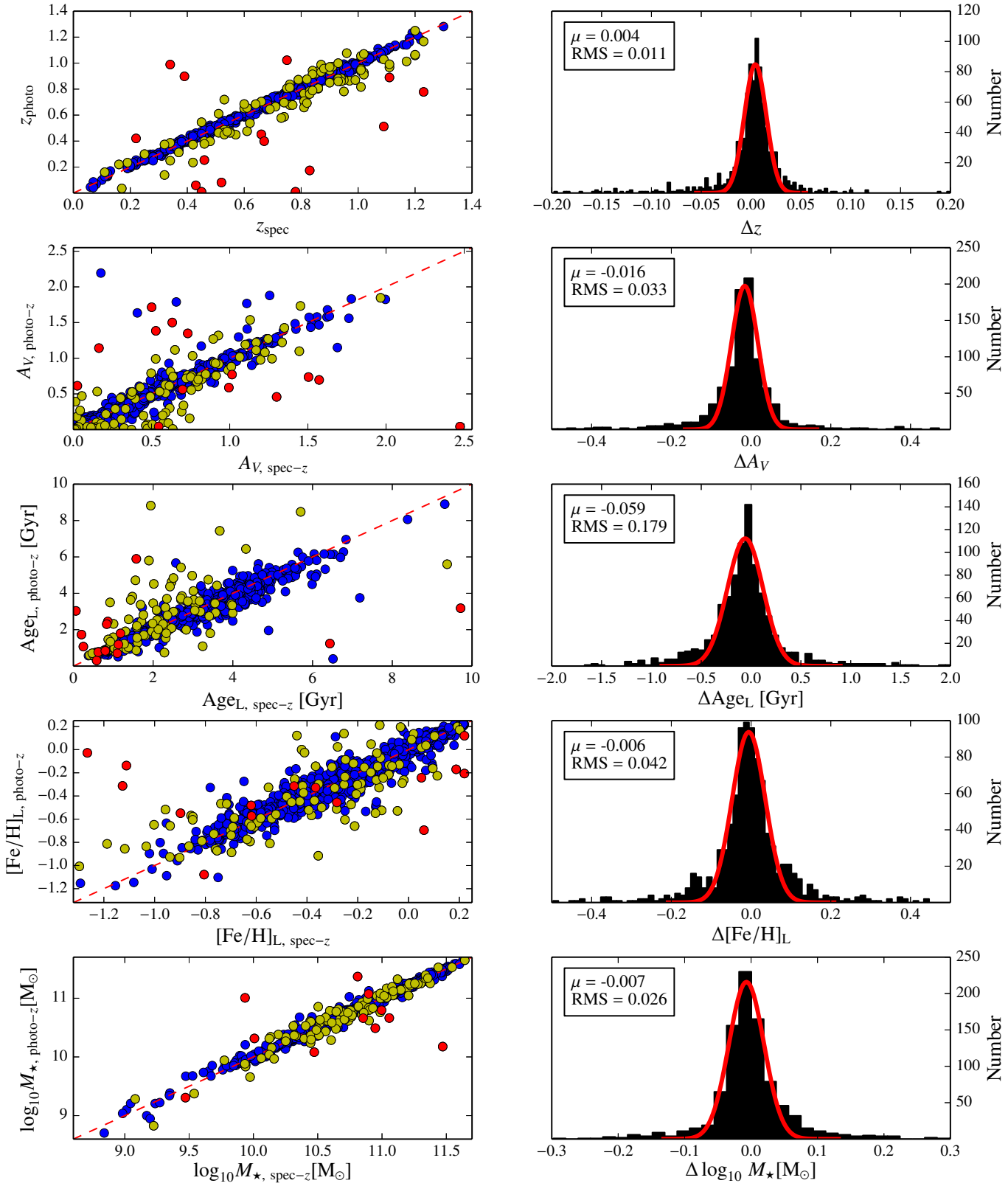

Fig. 10. Impact of a redshift uncertainty ∼1% on the stellar population parameters. On the left, we present the comparative one-to-one of the obtained parameters without any constrain in the photo z (Y-axis) versus the results forcing the redshift to its spectroscopic value (X-axis). The dashed red line represents the one-to-one relationship. Red, yellow, and blue dots are galaxies for which $|z_{\rm spec} - z_{\rm phot}| > 0.2$, $0.044 \leq |z_{\rm phot} - z_{\rm spec}| < 0.2$, and $|z_{\rm phot} - z_{\rm spec}| < 0.044$, respectively. On the right, we have the histograms of the differences between the obtained results with and without the spectroscopic constraint. The solid red line is the best fit of the distribution to a Gaussian function, and the boxes show both Gaussian mean and rms. *From top to bottom*, we show redshift, extinction, age, metallicity, and stellar mass.

the MIUSCAT SSP models. The degeneracy estimation is done by taking all the stellar population values recovered during the Monte Carlo approaches at different stellar population bins (detailed below), and then stacking each retrieved distribution to build a whole distribution per bin, getting distributions among pairs of parameters (age, metallicity, and extinction). We characterise each distribution by setting confidence ellipses (2D confidence intervals) that enclose the results provided during the Monte Carlo process. These ellipses are obtained by the covariance matrix of each distribution, and they allow parametrising the degeneracies through two parameters: by the ellipticity, denoted as e, and by θ, the angle between the X–axis and the ellipse semi-major axis.

The angle θ is determined by the eigenvectors of the covariance matrix, as well as the eigenvalues of the covariance matrix determine the axis lengths. If e is close to zero, this implies that the degeneration between the two parameters is not very significant, irrespective of the value of θ. On the other hand, if θ is a multiple of $\pi/2$ (lies on any of the two axes), both parameters are uncorrelated, consequently there is no degeneracy between them. Consequently, both parameters are necessary to confirm whether a degeneracy exists or not. In fact, we can quantify the level of degeneracy between parameters via the Pearson's correlation coefficient, which mathematically reflects both e and θ effects. Formally,

$$r_{xy} = \frac{\sum_{i=1}^{n}(x_i - \bar{x})(y_i - \bar{y})}{\sqrt{\sum_{i=1}^{n}(x_i - \bar{x})^2 \sum_{i=1}^{n}(y_i - \bar{y})^2}}, \quad (25)$$

where x_i and y_i denote the value pairs of the parameters (age, metallicity, extinction) with means $\bar{x}$ and $\bar{y}$, respectively. The closer r_{xy} is to 1 (to -1), the larger the correlation (anti-correlation), meaning the degeneracy between parameters; in contrast, a value close to 0 ($-0.1 \lesssim r_{xy} \lesssim 0.1$) suggests that the parameters are uncorrelated, and there would be no degeneracy.

Regarding the parameter ranges, we take bins in age of $0.5 \leq \mathrm{Age_L} \leq 1.0$, $3.0 \leq \mathrm{Age_L} \leq 4.5$, and $7.0 \leq \mathrm{Age_L} \leq 10.0$ Gyr, whereas for metallicity we take $-0.8 \leq [\mathrm{Fe/H}]_\mathrm{L} \leq -0.6$, $-0.4 \leq [\mathrm{Fe/H}]_\mathrm{L} \leq -0.2$, and $-0.1 \leq [\mathrm{Fe/H}]_\mathrm{L} \leq 0.1$. These bins have been chosen to evaluate how the degeneracies vary along different stellar population parameters. We do not establish any extinction bin, because we have previously checked that the degeneracies in different extinction bins present negligible differences in e and θ. We also studied whether different redshifts can alter the degeneracy effects, since the redshift determines the observed spectral range of the ALHAMBRA SEDs. We find that at higher redshift some degeneracies tend to decrease, especially for young and low-metallicity galaxies, but in general the degeneracies remain alike (less dispersion as well, see Sect. 4.2). Thus, the three bins in age and in metallicity define the nine intervals where the degeneracies of our parameters are explored. In each interval, we compare the age-metallicity, age-extinction, and metallicity-extinction degeneracies.

In Fig. 11 we present the covariance error ellipses (in blue) that enclose, at the 95% confidence level, the distribution of the provided parameters during the Monte Carlo approach for all the ALHAMBRA RS galaxies in the nine age and metallicity ranges (see inner panels), and at redshift $z \leq 0.4$. The semi-minor and semi-major axes of each ellipse are shown in red, whereas their centres are represented with a yellow square. Table 3 provides θ, e, and r_{xy} for the same age and metallicity regimes.

As intuitively expected, age and extinction are anti-correlated in all cases, in the sense that a reddening by extinction can mimic an older age, and vice versa. However, the behaviour of the age-metallicity and metallicity-extinction degeneracies is not so immediate. This is clearly a consequence of the role that extinction plays in the analysis as a third degree of freedom, partially absorbing the weight of metallicity in the classical age-metallicity degeneracy problem. Whilst older galaxies exhibit, as expected, clear anti-correlated age-metallicity and metallicity-extinction degeneracies, such anti-correlations may turn into very mild or even positive correlations depending on the range of age and metallicity. For instance, at the lower metallicity range, young and intermediate-age galaxies exhibit a positive degeneracy between age and metallicity, turning mild or negligible for young galaxies with intermediate and high metallicities. Interestingly, young metal-rich galaxies are essentially only subject to the extinction-age degeneracy.

Finally, we checked that the general degeneracy trends presented in this section do not vary qualitatively when computed on the basis of the BC03 models (see Table 3). For ages lower than ∼1 Gyr, there is a clear degeneracy of both age and metallicity with extinction, and for older ages, there is also an age-metallicity degeneracy.

5. Testing the perfomance of the code with ALHAMBRA galaxy data

Once the technical details of MUFFIT have been described in detail and the typical uncertainties and degeneracies amongst the derived parameters have been studied for the case of the ALHAMBRA survey, in this section we apply the code to different subsamples of galaxies in ALHAMBRA. The ultimate goal of this section is not to provide a thorough study of the stellar populations of ALHAMBRA galaxies, but rather to test the reliability of the stellar populations, emission line EW, stellar masses, and redshifts derived from our code in comparison with those published in previous work for either similar or identical galaxy samples. A forthcoming paper (Díaz-García et al., in prep.) will present a complete analysis of the stellar populations of galaxies in ALHAMBRA making use of MUFFIT.

5.1. Stellar masses and photo z in the COSMOS survey

Since Field 4 in the ALHAMBRA survey partly overlaps with the COSMOS field, we can construct a subsample of RS galaxies (see Sect. 4.1) in common between both surveys. After removing all the sources labelled as stars in COSMOS (point-like sources, Ilbert et al. 2009) and in ALHAMBRA, we end up with a subsample of 767 common galaxies up to redshift $z \leq 1.6$.

This galaxy subsample indeed has an important added value for our testing goals, because it has spectroscopic data in the zCOSMOS 10k-bright catalogue (Lilly et al. 2007, 2009), allowing for a calibration of the derived photo z using the Le PHARE code. In addition, using broad and medium bands and following a SED-fitting technique with BC03 models, Ilbert et al. (2010) estimated the stellar masses of the COSMOS galaxies. They assumed a fixed Chabrier IMF (similar to the IMF of Kroupa 2001), a star formation rate $\propto e^{-t/\tau}$ (with $0.1 \leq \tau \leq 30$ Gyr), a unique solar metallicity, an age grid of 0.1–14.5 Gyr, and the Calzetti et al. (2000) extinction law with $0.0 \leq E(B-V) \leq 0.5$.

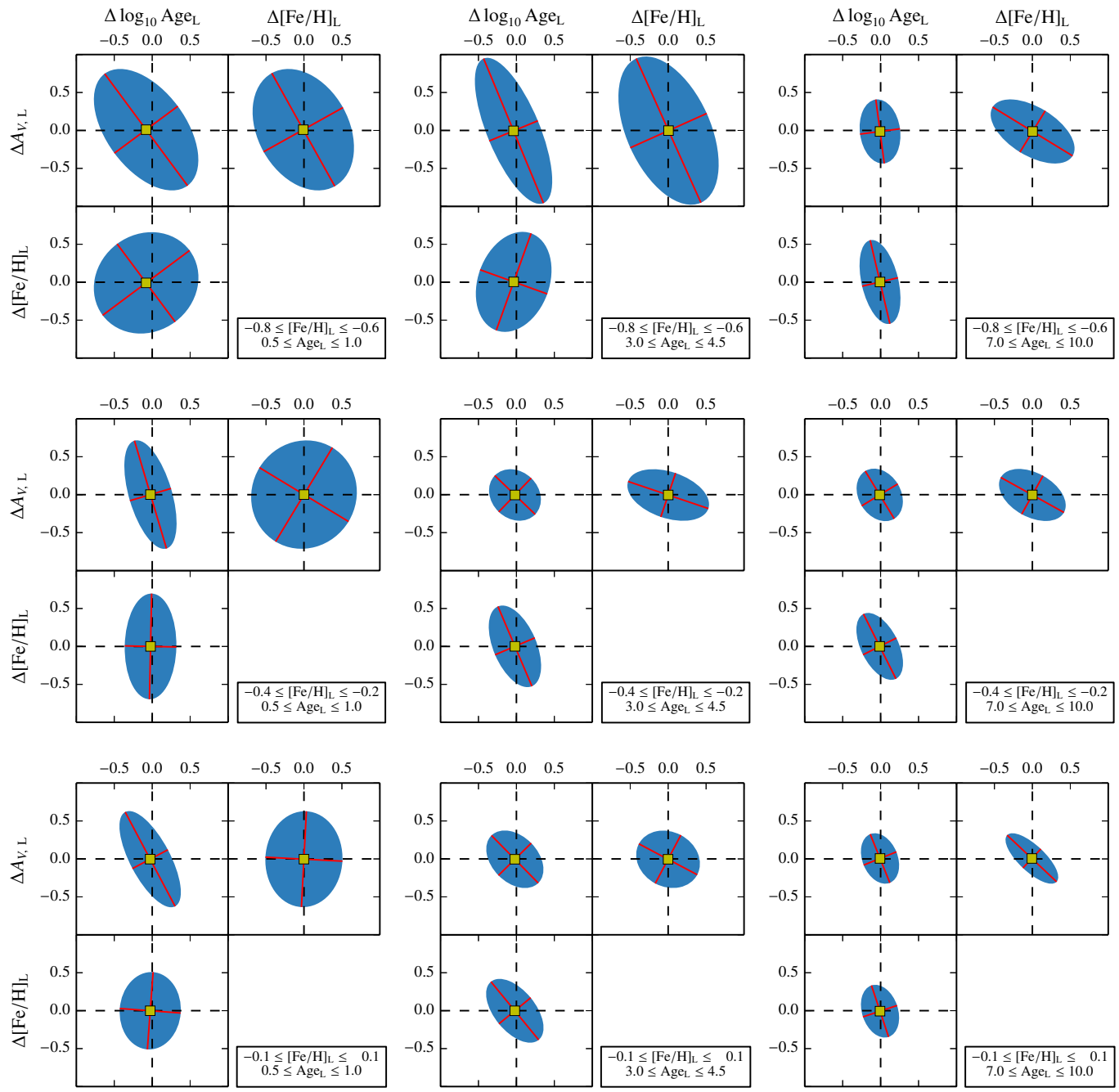

Fig. 11. Covariance error ellipses, at the 95% confidence level, of the stellar population parameters provided by the Monte Carlo approach in MUFFIT with respect to their most probable values, for different age and metallicity bins (see *inner panels*). Yellow squares indicate the ellipse centres, and the red lines illustrate the minor and major axes of each ellipse.

(High extinction values are only allowed for galaxies with high star formation.)

For analysing this sample we used MUFFIT, which imposes a mixture of two SSPs rather than an exponential star formation rate. We selected MIUSCAT models with a Kroupa IMF (which slightly differs from the Chabrier IMF), for a wider range in metallicity ($-1.31 \leq [\mathrm{Fe/H}] \leq 0.22$). For our analysis we used the Fitzpatrick (1999) extinction law rather than the Calzetti et al. (2000) law, because the latter is generally more appropriate to central star-forming regions (Calzetti 1997).

In Fig. 12 we present a one-to-one comparison of the photo-z and stellar masses obtained with our code on the ALHAMBRA data and those presented in the above work on the COSMOS data (Ilbert et al. 2009, 2010) for the subsample of 767 RS galaxies in common. Having already constrained the reliability and accuracy of the ALHAMBRA photo z with respect to available spectroscopic redshifts (see Sects. 4.3 and 4.4), in the top panels of Fig. 12, we compare our outcomes with the COSMOS photo z, not only because of the qualitative similarity of both techniques, but also to check that there are systematics in our photo-z measurements that might cause any kind of systematic in the retrieved ALHAMBRA stellar masses. From these plots we can see that both photo-z estimations are in very good agreement, with one-to-one differences having an rms of just 0.015, and not finding statistically significant differences between both samples. The bottom panels of Fig. 12 are devoted to the stellar mass

Table 3. Summary of the confidence error ellipses in Fig. 11 for different parameter bins and MIUSCAT (top) and BC03 (bottom) models.

		0.5 ≤ Age [Gyr] ≤ 1.0			3.0 ≤ Age [Gyr] ≤ 4.5			7.0 ≤ Age [Gyr] ≤ 10.0		
		r_{xy}	θ	e	r_{xy}	θ	e	r_{xy}	θ	e
MIUSCAT	$\Delta\log_{10}$ Age vs. Δ[Fe/H]									
	$-0.8 \leq$ [Fe/H] ≤ -0.6	0.11	36	0.11	0.24	70	0.31	−0.40	103	0.58
	$-0.4 \leq$ [Fe/H] ≤ -0.2	0.03	88	0.52	−0.49	113	0.51	−0.51	116	0.50
	$-0.1 \leq$ [Fe/H] ≤ 0.1	0.04	85	0.22	−0.55	129	0.46	−0.26	108	0.35
	Δ[Fe/H] vs. ΔA_V									
	$-0.8 \leq$ [Fe/H] ≤ -0.6	−0.30	119	0.30	−0.46	114	0.47	−0.54	148	0.49
	$-0.4 \leq$ [Fe/H] ≤ -0.2	0.05	58	0.05	−0.37	161	0.46	−0.41	150	0.40
	$-0.1 \leq$ [Fe/H] ≤ 0.1	0.02	87	0.20	−0.16	152	0.18	−0.76	136	0.63
	$\Delta\log_{10}$ Age vs. ΔA_V									
	$-0.8 \leq$ [Fe/H] ≤ -0.6	−0.50	126	0.44	−0.69	112	0.67	−0.13	97	0.38
	$-0.4 \leq$ [Fe/H] ≤ -0.2	−0.53	106	0.63	−0.18	136	0.17	−0.25	121	0.25
	$-0.1 \leq$ [Fe/H] ≤ 0.1	−0.70	117	0.63	−0.37	134	0.32	−0.28	111	0.34
BC03	$\Delta\log_{10}$ Age vs. Δ[Fe/H]									
	$-0.8 \leq$ [Fe/H] ≤ -0.6	−0.07	93	0.42	−0.24	104	0.38	−0.19	96	0.53
	$-0.4 \leq$ [Fe/H] ≤ -0.2	0.01	89	0.39	−0.46	112	0.49	−0.32	120	0.31
	$-0.1 \leq$ [Fe/H] ≤ 0.1	−0.05	91	0.54	−0.57	118	0.53	−0.48	136	0.41
	Δ[Fe/H] vs. ΔA_V									
	$-0.8 \leq$ [Fe/H] ≤ -0.6	−0.63	145	0.55	−0.22	118	0.23	−0.77	150	0.68
	$-0.4 \leq$ [Fe/H] ≤ -0.2	−0.58	141	0.49	−0.16	167	0.31	−0.34	158	0.40
	$-0.1 \leq$ [Fe/H] ≤ 0.1	−0.59	144	0.51	−0.10	174	0.37	−0.25	104	0.39
	$\Delta\log_{10}$ Age vs. ΔA_V									
	$-0.8 \leq$ [Fe/H] ≤ -0.6	−0.45	118	0.43	−0.62	114	0.60	−0.16	104	0.28
	$-0.4 \leq$ [Fe/H] ≤ -0.2	−0.50	117	0.48	−0.43	126	0.38	−0.46	144	0.41
	$-0.1 \leq$ [Fe/H] ≤ 0.1	−0.46	108	0.53	−0.40	140	0.35	−0.44	116	0.44

Notes. θ is the angle between the X-axis and the semi-major axis a in degrees (counter clockwise), whereas e is the ellipticity. To quantify the degeneracy between parameters, we provide the Pearson's correlation coefficient, r_{xy}, where values close to 0 correspond to uncorrelated parameters.

comparison. We find that the mean value of the one-to-one stellar mass differences is 0.04 dex, with a dispersion of 0.15 dex.

As we explained in Sect.4.4, the typical uncertainties of our ALHAMBRA photo z may have an impact on the dispersion of the retrieved stellar masses of up to 0.026 (see Fig. 10), well below the observed value. On the other hand, the offset between masses cannot be completely explained by the mild offset between redshifts ($\mu = 0.005$), since when using Eq. (15), this difference implies a shift in mass $\lesssim$0.015 dex. Previous work have already reported the non-negligible effect of using different model sets on the absolute values of the derived stellar masses (see e.g. Pozzetti et al. 2007; Ilbert et al. 2010). To check this in our particular case, we have repeated the above analysis for the same subsample of galaxies with the BC03 models, instead of MIUSCAT. The new mean difference between the stellar masses of ALHAMBRA and COSMOS galaxies is now −0.03 dex, with a similar dispersion of rms = 0.15 dex. Consequently, the mild systematic between stellar masses is probably due to the SSP model choice. Irrespective of the input set of SSP models, the dispersion between the stellar masses provided by COSMOS and the retrieved from ALHAMBRA data after running MUFFIT remains rms $\sim$ 0.15 dex. This can be easily explained as the quadratic sum of the stellar mass uncertainties retrieved from both COSMOS and our proper technique in the common sample, where ∼0.09 dex in COSMOS and ∼0.11 dex in ALHAMBRA.

As a general conclusion, despite the differences in the analysis techniques presented in this paper for ALHAMBRA galaxies and those performed by previous work for the COSMOS data, we find remarkable agreement between the photo-z and the stellar masses derived for galaxies in common, showing the reliability and robustness of our code. We confirm that the choice of SSP models and extinction laws has an impact on the absolute values of the derived stellar masses. In particular, we find that the stellar masses derived using the MIUSCAT models lead to mean values of 0.07 dex that are higher than when using BC03 models.

5.2. Photometric EWs of emission lines

During the SED fitting process, the detection and subsequent removal of the bands affected by nebular emission lines may be crucial for determining reliable properties of the underlying stellar content of the galaxy under study. The way in which the affected bands are detected and removed from the analysis is

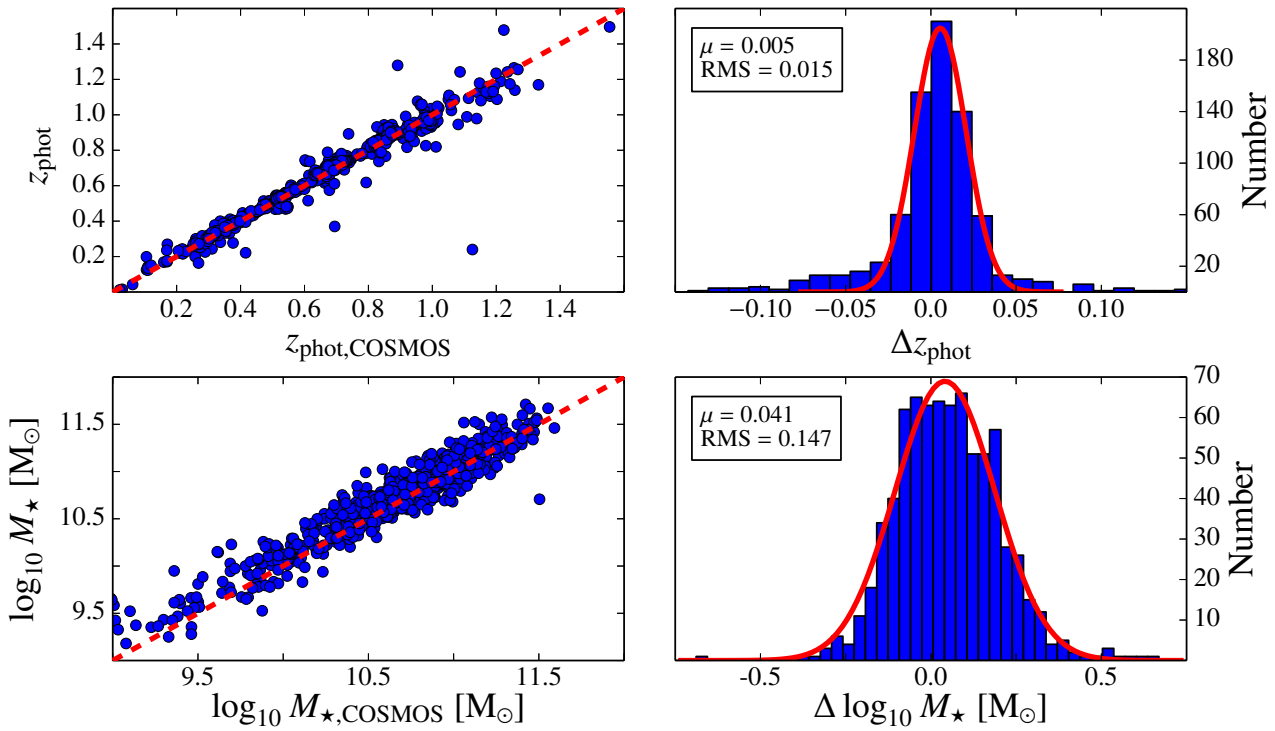

Fig. 12. Differences between the photo-z (*top panels*) and stellar masses (*bottom panels*), computed with MUFFIT (Y-axis) and the values provided in COSMOS catalogues (X-axis; Ilbert et al. 2009, 2010), for a subsample of RS galaxies. On the right, we show the histograms of the differences, which are fitted to a Gaussian distribution.

already described in Sect. 3.2.2. Here we analyse to what extent the emission line residuals retrieved from our fittings, based on photometric data, are reliable and still keep meaningful information on the true EWs of the nebular lines derived from classical spectroscopy.

To build up a comparison galaxy sample, we first take all the ALHAMBRA galaxies that i) are in common with the data catalogues of the MPA/JHU[9] (hereafter MPA/JHU catalogues) and ii) present nebular emission lines in their spectra (Brinchmann et al. 2004; Tremonti et al. 2004). This catalogue contains EWs and flux measurements of nebular lines for galaxies in the SDSS DR7 (Abazajian et al. 2009). Such measurements already account for their corresponding underlying stellar absorptions, because they were calculated after subtracting appropriate SSP models.

Since our stellar population code is focused on the analysis of galaxies whose SEDs are dominated by their stellar content, for a fair comparison we systematically remove all the AGNs and QSOs from the sample (*AGN*, *AGN_BROADLINE*, *QSO*, and *T2* types in SDSS), even if some of them could still be interpreted by our code. In addition, galaxies with a signal-to-noise ratio lower than 5 in the EW continuum are removed, as are those galaxies in the redshift ranges $0.112 < z < 0.114$, $0.123 < z < 0.125$, and $0.146 < z < 0.148$, to avoid EW contaminations due to the sky line O I λ5577, and all the galaxies larger than 4″ (the SDSS fibres have 3″ diameter) to minimise strong aperture effects in the photometry. Under the above constraints, there are 92 galaxies in common between ALHAMBRA and the MPA/JHU catalogues of SDSS.

The detection and classification of emission lines in multi-filter surveys is clearly limited by the low spectral resolution of the data. For instance, at the ALHAMBRA resolution, and depending on the redshift, the emission line pairs Hβ-[O III], Hα-[N II], and even Hα-[S II] can be unresolved because of their proximity in wavelength. To try to overcome this intrinsic limitation, rather than comparing the EWs of individual lines, we compare the total flux in excess along the observed spectral-range ($\lambda\lambda$ 3500–9700 Å for ALHAMBRA) with the total sum of the EWs measured in the MPA/JHU catalogues for the following strong nebular lines: Hβ λ4861, [O III] λ4959, [O III] λ5007, Hα λ6563, [N II] λ6548, [N II] λ6584, [S II] λ6717, and [S II] λ6731. We do not account for weaker lines because they might not be detected under the ALHAMBRA resolution. As explained in Sect. 3.2.2, we set the detection limits of emission lines in ALHAMBRA to a flux excess of $\Delta m_{\rm EL} = 0.1$ and a signal-to-noise ratio with respect to the photometric error of the filter of $\sigma_{\rm EL} = 2.5$. Out of the 92 galaxies in common, there are 44 galaxies in ALHAMBRA for which our code detects an emission line in at least one filter, hence constituting the final galaxy subsample for the sake of EW comparisons.

Since our SED-fitting technique is based on a χ^2 minimization technique between the filter fluxes of models and real galaxies over the full spectral range of the data, we must be aware that the best fitting solution may not match the local continuum around the emission lines perfectly, leading to random over- or under-estimations of the flux line. To minimise this effect for the sake of this study, given the filter that contains the emission line, f_l, we define a local continuum for this band, f_l^c, as the mean value of the flux in the contiguous bands not affected by the emission line. For the model band that contains the modelled corresponding stellar absorption, t_l, we similarly define a continuum for the model, t_l^c, in the same bands as where f_l^c is calculated. Following the formalism for spectroscopic EWs, the equation for photometric EWs (in Å) is

$$EW_{\rm T,phot} = \sum_X \left(\frac{f_l}{f_l^c} - \frac{t_l}{t_l^c} \right) \Delta\lambda_l, \qquad (26)$$

[9] www.mpa-garching.mpg.de/SDSS/

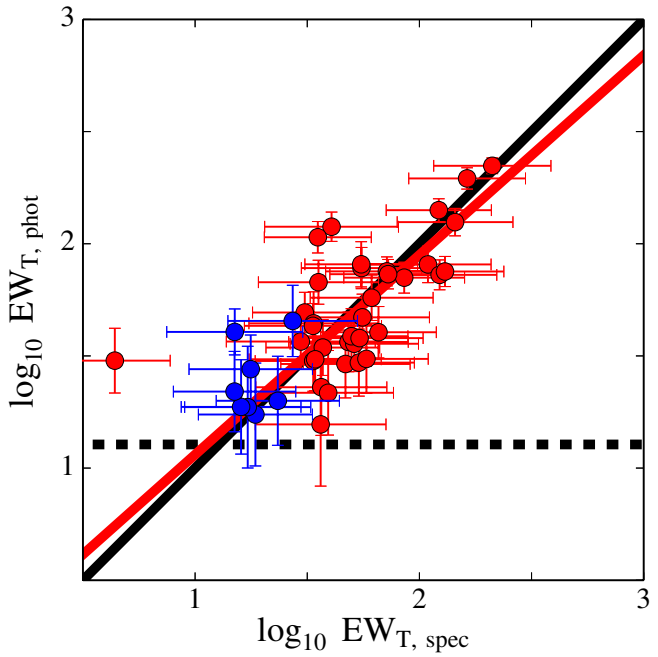

Fig. 13. Comparison between the emission line EWs measured in galactic SDSS spectroscopic data taken from the MPA/JHU catalogues, $EW_{\rm T,\ spec}$, and the emission line EWs derived from the residuals of our fitting code on the same galaxies in ALHAMBRA, $EW_{\rm T,\ phot}$. Blue dots indicate galaxies with only one strong emission line in their spectra, i.e. with a reasonably specific or individual emission line measurement in ALHAMBRA, whereas red dots illustrate galaxies with more than one emission line. The black line is the one-to-one relationship, whereas the red line is a linear regression to all the points. The dashed black line is the minimum $EW_{\rm T,\ phot}$ that we can detect when imposing $\Delta m_{\rm EL} = 0.1$ for a unique emission line in one ALHAMBRA filter. See more details in the text.

where $\Delta\lambda_l$ is the width of the band (~300 Å for the optical filters in ALHAMBRA) that contains the emission line, and the sum applies to all the bands affected by strong emission lines, X.

In Fig. 13 we present the photometric $EW_{\rm T,\ phot}$ derived with our spectral-fitting techniques on ALHAMBRA data versus the spectroscopic $EW_{\rm T,\ spec}$ computed from MPA/JHU catalogues, for the 44 galaxies in common that fulfilled the above selection criteria. Overall, we obtain good agreement between photometric and spectroscopic EWs considering both photometric and spectroscopic uncertainties (see the red line), where the bias between both measurements is $\mu = 0.018$ dex and rms = 0.234 dex, demonstrating the feasibility and reliability of our code for determining the EWs of emission lines above a certain strength ($\gtrsim$13 Å). We highlight that the concordance with our photometric EW predictions is good independently if the galaxies only present one strong emission line in their spectra (blue dots) or they present more than one emission line (red dots) in SDSS. It is interesting that under the imposed detection limit $\Delta m_{\rm EL} = 0.1$ (dashed black line), there is no detection of emission lines either. In fact, our method can provide more robust determinations under certain conditions. This is the case, for instance, for the galaxy that deviates on the left-hand side of the panel. The SDSS spectrum of this galaxy, at redshift $z = 0.299$, exhibits both Hα and Hβ in emission. Hβ emission is too weak to be detected in ALHAMBRA with our criteria, whilst Hα, at λ8526, falls in a very noisy region of the spectrum plenty of sky emission line residuals and telluric bands, which are hardly corrected in the SDSS data. This is not the case for the ALHAMBRA data, for which the continuum is better determined and where the absolute flux excess, for this particular case, becomes more reliable.

Finally we pay attention to the 48 galaxies for which our code does not detect any emission line in the ALHAMBRA data with the detection limits set in this paper. We find that 35 galaxies (~75%) present $\log_{10} EW_{\rm T,\ spec} \leq 1.11$ (~13 Å), which corresponds to our detection limit $\Delta m_{\rm EL} = 0.1$, i.e. that indeed remain imperceptible under our detection constrain. Of the remaining 13 galaxies, ten have $\log_{10} EW_{\rm T,\ spec} > 1.11$, but distributed along different lines, where all the lines individually are under the detection limit. Finally, for three galaxies we did not properly detect the emission lines for two reasons: first, since one of the emission lines (in this particular case Hα) is right between two filters and the flux is split into both of them, not fulfilling the detection criteria in any of the filters. Second, there was an incorrect determination of the $z_{\rm phot}$, which prevents the code from looking for emission lines in the right filters, besides the fact that a wrong redshift determination affects the quality of the derived continuum, yielding a line residual under $\Delta m_{\rm EL} = 0.1$.

To conclude, we demonstrate that despite MUFFIT being mainly optimized for the analysis of the stellar populations of galaxies dominated by their stellar content, it is still reliable for detecting and characterising the strength of strong emission lines under certain conditions that depend on the type of the multi-filter data we are working with (e.g. filter width, signal-to-noise ratios per filter). In future versions of the code, we expect to improve the algorithms of detection of emission lines with additional techniques and criteria (e.g. assuming intrinsic relations among lines), but this is beyond the scope of the present paper.

5.3. The stellar populations of M32

As a first step in testing the reliability of the stellar populations derived with our code, we analysed the stellar content of M32, because this is one of the best known galaxies in terms of its resolved and unresolved stellar populations. The spectrum of M32 used for this study was taken from the compilation of Santos et al. (2002), and it had been convolved with the ALHAMBRA filter set for the sake of this test, as if it had been observed in ALHAMBRA. Since the spectral range of this spectrum, $\lambda\lambda$ 3500–10 000 Å, is shorter than the filter coverage of ALHAMBRA, both the bluest optical filter and the three NIR filters were rejected from the whole fitting procedure described in Sect. 3. In addition, to be able to explore the parameter space that is compatible with the best solution due to uncertainties in the photometry, and given that we had created a fake ALHAMBRA spectrum from a higher resolution spectrum, we added a synthetic error of $\sigma_{\rm AB} = 0.025$ in each filter, which is the expected error in the photometric calibration of ALHAMBRA (equivalent to a signal-to-noise ratio ~40).

In Fig. 14 we present the complete spectrum of M32, in black, the M32 spectrum at the ALHAMBRA resolution and the best fit derived from our code with a mixture of two MIUSCAT SSPs and a Kroupa IMF to the M32 ALHAMBRA spectrum. As consequence of the spectral range ($\lambda\lambda$ 3500–10 000 Å), the bluest and NIR ALHAMBRA filters were rejected in the analysis. The obtained residuals are shown in the lower panel.

It is clear from Fig. 14 that the best fit derived from our code reproduces the observed spectrum well at both low and high frequencies. The best fitting solution to a single SSP, as derived from our code in the first step, corresponds to a MIUSCAT model of 3.7 ± 1.3 Gyr and around solar metallicity ([Fe/H] = 0.02 ± 0.14 dex). When the code was run completely for the

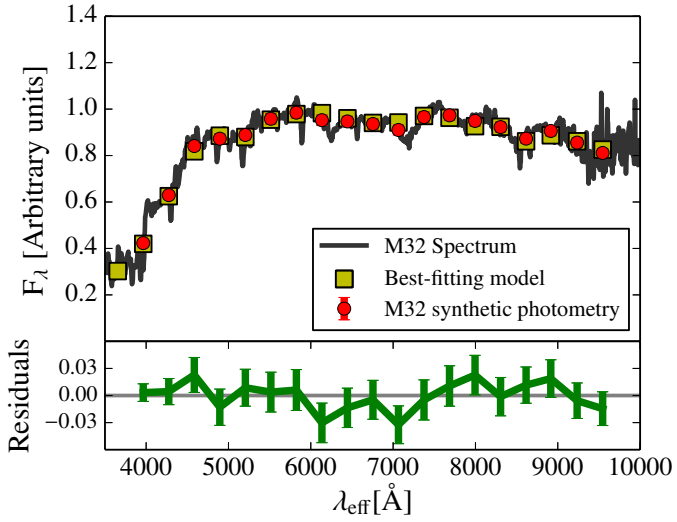

Fig. 14. Spectral fitting of M32 as seen by ALHAMBRA using the MIUSCAT SSP SEDs as template models with the analysis explained above. The synthetic photometry of M32 is plotted in red, whereas the best fit of a mixture of two SSPs to the spectrum of M32 is plotted in yellow. The *bottom pannel* shows the residuals of the best fit.

mixture of two SSPs, we obtained a luminosity-weighted age of 6.8 ± 2.2 Gyr, a slightly sub-solar metallicity ([Fe/H] = −0.08 ± 0.14 dex), and extinction $A_V = 0.28 \pm 0.08$. Looking at the individual results for the two SSPs, we find that the spectrum of M32 is appropriately reproduced by an intermediate-age population of 2.1 ± 0.5 Gyr and an older population of 11.5 ± 3.4 Gyr. We find that the weight on the stellar mass of the young population is ∼20%. Previous work, such as from Coelho et al. (2009) and Monachesi et al. (2012), arrive at similar results in the sense that M32 is not composed of a unique SSP of intermediate age, but its stars were formed in at least two episodes of star formation, one ancient and the other one at intermediate ages.

Even though we are using 19 filters (instead of 23 in a typical ALHAMBRA photo-spectrum), we still get good agreement between the retrieved parameters and those derived by previous work when making use of detailed spectroscopic studies, showing the power of this kind of multi-filter survey for stellar population studies.

5.4. Ages and metallicities of early-types in the local Universe

Disentangling the stellar populations of early-type galaxies and their assembling histories is a key question for our understanding of galaxy evolution; however, it is not our intention to address this point in this section. The aim of this section is only to explore the stellar content of a subsample of early-type galaxies in the nearby Universe from the ALHAMBRA survey, making use of MUFFIT, and to compare our results with previous findings in the literature. Once again, this is an additional check to assess the reliability of the stellar populations derived from our techniques. In a forthcoming paper (Díaz-García et al., in prep.), we will carry out a more complete and systematic analysis of all the galaxies in ALHAMBRA, allowing us to face these and other related questions.

Our reference work is the paper by Gallazzi et al. (2005, in the following G05) and, in particular, the ages and metallicities derived from spectroscopic analysis techniques for a sample of early-type galaxies located at $z < 0.22$ in SDSS. Their spectra were drawn from the SDSS DR4 (3″ diameter fibres, Adelman-McCarthy et al. 2006) spanning the full range of galaxy types (from actively star-forming to early-type galaxies) and covering the range $\lambda\lambda$ 3800–9200 Å with a resolution of $R \sim 1800$, and Petrosian magnitudes in the r-band range $14.5 < r < 17.77$. To construct our subsample of early-types galaxies in ALHAMBRA we have used the morphological catalogue provided by Pović et al. (2013), built using the code galSVM (designed to deal with low-resolution images at low and high redshifts, Huertas-Company et al. 2008) that, following a Bayesian approach, classifies the galaxies morphologically. This catalogue contains more than ∼1500 early-type galaxies with redshifts down to $z \lesssim 0.5$ and a contamination lower than 10%, up to magnitude $m_{F613W} \leq 22$. To guarantee a fair comparison study, we only select those early-type galaxies in ALHAMBRA with $z \leq 0.22$ from the above catalogue, so in the same redshift interval as in G05. With this constraint in redshift, we end up with a reliable subsample of ∼400 early-type galaxies (mean signal-to-noise ratios $S/N > 14$ in all cases), in which a significant part (∼65%) also reside in the RS.

Following Fig. 12 in G05, in Fig.15 we present the density contours of our results on luminosity-weighted ages, $\mathrm{Age_L}$, and metallicities, $\mathrm{[Fe/H]_L}$, derived for our subsample of early-type galaxies in ALHAMBRA up to $z = 0.22$ using BC03 models and the photo-z constraints provided by the Gold catalogue. As in G05, the galaxy sample is split in stellar mass bins as indicated in the top labels of Fig. 15. For each galaxy, rather than using the weighted values retrieved from the simulations, the whole set of results from the Monte Carlo simulations (see Sect. 3.2.5) are included in the plot. Darker colours correspond to the ages and metallicity regions with higher population densities. To see the influence of the age-metallicity degeneracy on the results, we also include the semi-axes of the degeneracy ellipses for 1σ confidence level for the BC03 SSP models, as computed in Sect. 4.5, in the same age and metallicity ranges.

From a purely comparative point of view, the similarity of the age and metallicity results derived from our code and the ones presented in Fig. 12 of G05 on the basis of totally different spectroscopic analysis techniques is highly remarkable. This is an excellent proof that the reliability of the stellar population techniques presented in this paper for analysing multi-filter galaxy data is comparable to the ones employed during recent decades for analysing spectroscopic data, like diagnostic diagrams based on line-strength indices, at least when they were applied to large volumes of data.

From Fig. 15 we infer that low-mass early types, $\log_{10} M_\star \lesssim 10.3$ dex, show a bimodal distribution in their stellar populations. There is a population of younger early types with slightly lower metallicities that does not seem to exist at higher masses. On the other hand, there is a main population of older and, on average, more metal-rich galaxies at the same stellar mass bin. The set of younger early types of mild metallicities may be contaminated by lenticular galaxies (Poggianti et al. 2001), and they are also found in G05. Using the rest-frame colours (see Sect. 3.2.6), we check that almost the totality of these "young" galaxies corresponds to galaxies that reside in the blue cloud, and they are probably composed mainly of star-forming bulge-dominated galaxies.

It is worth noticing that, even though this analysis is based on photometric data, using MUFFIT and ALHAMBRA allows us to be sensitive to this population and to characterise their stellar populations quite well by not only obtaining close agreement with spectroscopic studies, but also opening the possibility of extending the mass limit up to lower stellar masses than typical

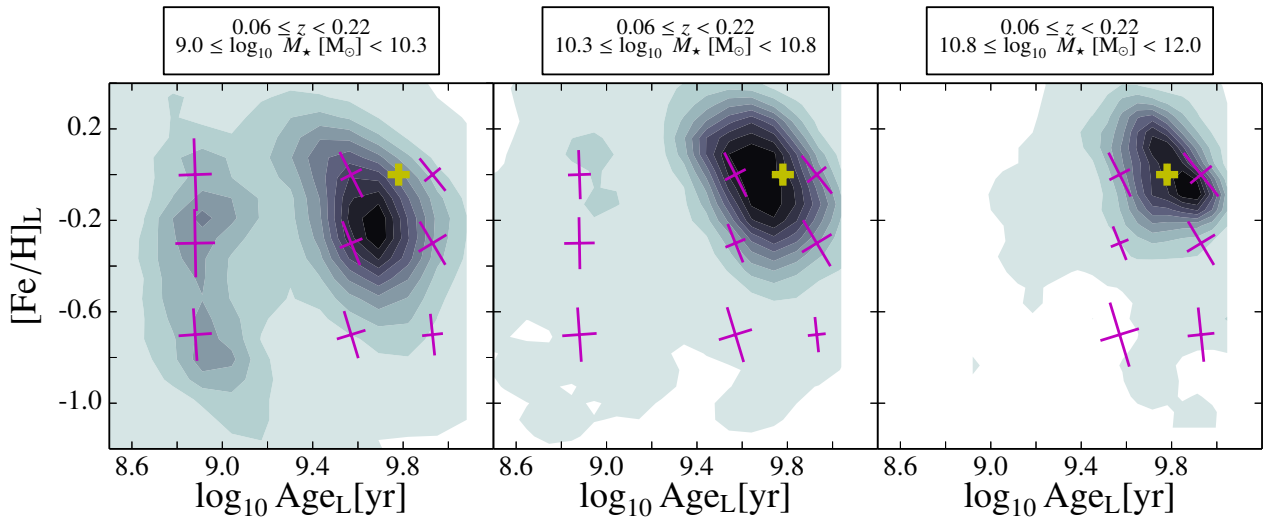

Fig. 15. Luminosity-weighted ages and metallicities derived from MUFFIT and the BC03 models, for a subsample of ALHAMBRA early-type galaxies at different stellar mass bins and up to $z \leq 0.22$. Purple crosses illustrate the semi-axes of the degeneracy ellipses for 1σ confidence level for the BC03 SSP models, as computed in Sect. 4.5, in the same age and metallicites ranges. To guide the eye, yellow crosses illustrate an age of 6 Gyr with solar metallicity.

spectroscopic surveys. We reinforce this result by repeating the analysis using the MIUSCAT SSP models instead of the BC03, getting the same result. Since the detailed analysis of the stellar populations is beyond the scope of this paper, this point will be addressed in a forthcoming work (Díaz-García et al., in prep.).

For intermediate stellar masses ($10.3 \lesssim \log_{10} M_\star[M_\odot] \lesssim 10.8$), the "young" population tends to disappear, and consequently, the number of youngish and less metal-rich galaxies decreases, because they negligible for the higher stellar masses ($10.8 \lesssim \log_{10} M_\star[M_\odot] \lesssim 12.0$), for which there is a clear predominance of old and metal-rich galaxies. For the lowest stellar masses, the spread in age and metallicity is apparently larger than for the most massive cases. Overall, our results suggest that massive galaxies are on average more metal-rich than less massive ones (Tremonti et al. 2004; Gallazzi et al. 2005, 2006), therefore the abundance of metals in a galaxy is related or linked to its stellar mass, showing a wider spread at the low-mass end (also found in G05), except for the young metal-poor population. We also observe that the mean ages of massive early types tend to be slightly older than their less massive counterparts, so they were formed at earlier epochs (higher redshifts) than the low-mass galaxies, in agreement with the "downsizing" scenario (Cowie et al. 1996; Jimenez et al. 2007). The increase in the mean ages and metallicities for massive early types was also found in G05 (equivalent results with very similar age-metallicity relations using SDSS spectroscopy). Even though these stellar population differences are quite mild for the early-type galaxies (at least in comparison with late-type galaxies, see G05), it is worth pointing out that when running on the ALHAMBRA data, MUFFIT is still sensitive to the subtle changes in age and metallicity. On average, for the whole galaxy population in Fig. 15, we find that the increase in age from the low-mass galaxies ($9.0 \lesssim \log_{10} M_\star[M_\odot] \lesssim 10.3$) up to the most massive ones ($10.8 \lesssim \log_{10} M_\star[M_\odot] \lesssim 12.0$) is ~3 Gyr, with mean ages of 3 and 6 Gyr, respectively. Similarly, the mean metallicity progressively increases from −0.35 to about solar metallicity.

We performed several tests to assess whether the bi-modality in the populations of the less massive galaxies, $9.0 \leq \log_{10} M_\star < 10.3$ dex, is driven by age-metallicity degeneracies. First, we observed the degeneracies on the age-metallicity parameters for the whole sample of RS galaxies in ALHAMBRA at the parameter ranges of both distributions (Sect. 4.5, see Fig. 11 and Table 3). For both sub-populations ($\mathrm{Age_L} \sim 0.8$ Gyr with $[\mathrm{Fe/H}]_\mathrm{L} \sim -0.7$ dex; $\mathrm{Age_L} \sim 4$ Gyr with solar metallicity), the degeneracy contours do not present bi-modalities, and they are well constrained by a unique ellipse (illustrated in Fig. 15). In addition, we confirmed that all the Monte Carlo realisations of each individual galaxy in the left-hand panel of Fig. 15 clearly belong to only one of the two galaxy sub-populations, proving that degeneracies are not responsible for the younger and less metal-rich population at the low-mass regime. Moreover, we added noise ($\sigma_\mathrm{AB} = 0.05$–$0.20$, corresponding to a signal-to-noise ratio $S/N \sim 20$–5) to the high-mass galaxy sample and analysed them again with MUFFIT to see if there is any hint of bi-modality driven by degeneracies in low signal-to-noise regimes. Even in the worst case ($S/N \sim 5$), fewer than 3% of the galaxies end up in the young and metal poor sub-population region, without exhibiting any bimodal pattern in the distribution. We conclude that there is a true sub-population of "young" early-type galaxies in the stellar mass regime $9.0 \leq \log_{10} M_\star < 10.3$ dex, which is not a consequence of parameter degeneracies and the use of probability distribution functions.

5.5. Comparison with spectroscopic stellar-population studies

A definitive step forward in the above analysis rests on the one-to-one comparison of spectroscopic galaxy ages and metallicities with the ones derived from MUFFIT. Interestingly, there is a sub-sample of galaxies in the MPA/JHU catalogues for which individual spectroscopic estimations of ages and metallicities are provided (obtained following the methodology explained in G05), and also imaged in the ALHAMBRA fields. G05 performed an age and metallicity diagnostic method based on a simultaneous fitting to five absorption line strength indices, most of them in the Lick system (Gorgas et al. 1993; Worthey et al. 1994). They are made up of age-sensitive indices like D4000 (Balogh et al. 1999), Hβ and Hδ_A+Hγ_A, and by metal-sensitive indices like [$\mathrm{Mg_2}$Fe] (Bruzual & Charlot 2003) and

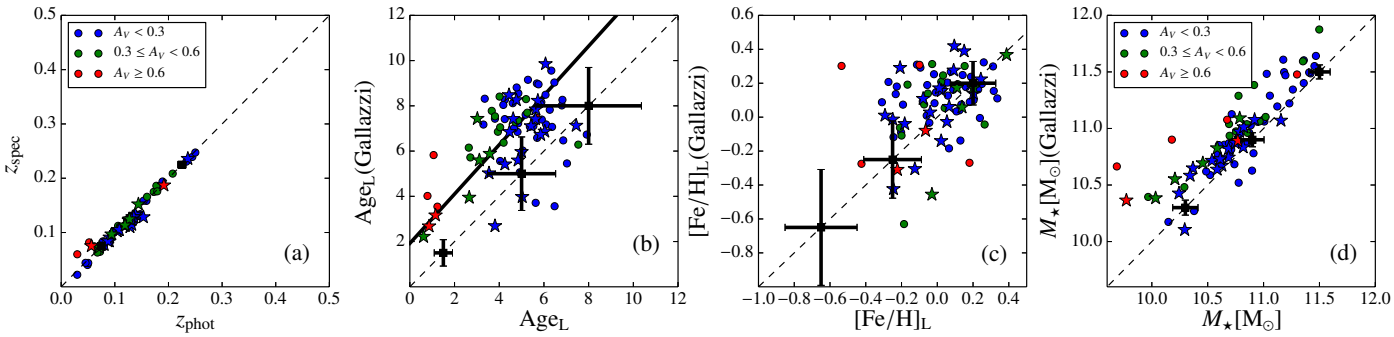

Fig. 16. Comparison of redshifts, ages, metallicities, and stellar masses between the spectroscopic study of Gallazzi et al. (2005), *Y*-axis, and the stellar populations retrieved from ALHAMBRA with BC03 models, *X*-axis. In red, we present the galaxies for which our techniques establish that they may have large extinctions: intermediate extinctions in green and low extinctions in blue. The dashed black line indicates the one-to-one relationship. The solid black line shows the fit between spectroscopic and photometric ages, accounting for the uncertainties in both measurements. The black crosses represent the average uncertainties of both techniques at different ranges. The star-shape markers are the galaxies with a radial size below 2″.

[MgFe]′ (Thomas et al. 2003), the latter weakly dependent on non-solar [α/Fe] abundances. Each set of five spectral features is compared, through a χ^2-test, with the values provided by a set of models randomly generated from BC03, with different bursts of star formation and different fractions relative to the total stellar mass in a velocity dispersion range, to finally construct the PDF of the parameters being the weight of each model $\propto\exp(-\chi^2/2)$ (see details in G05).

By crossmatching the ALHAMBRA galaxy catalogue with the above work, we find 80 RS galaxies (not spectroscopically classified as either *BROADLINE* or *AGN*) in common between both studies, with a mean signal-to-noise ratio per pixel in SDSS greater than nine. (Under this constraint, the signal-to-noise ratio of the common ALHAMBRA galaxies is more than 18 in all cases.) We establish this as a minimum threshold for obtaining meaningful stellar population results from spectroscopic diagnostics based on line-strength indices. Even if G05 stated that metallicity is well constrained for spectra whose signal-to-noise ratio is higher than 20, this more permissive restriction in the SDSS signal-to-noise ratio increases the number of common galaxies, allowing us to explore the age compatibility of both methods for a larger number of RS galaxies, where the age accuracy is not as affected by the signal-to-noise ratio of the SDSS spectra. (These details are extensively tested in G05.)

To keep the model consistent with G05, we fed MUFFIT with the SSP models of BC03 to explore, via ALHAMBRA data, the stellar content of these 80 RS galaxies in common. In addition, to explore the impact of different SSP models on the retrieved parameters, we repeated the same analysis with the MIUSCAT SSP models instead (see the end of this section).

Figure 16 presents a one-to-one comparison of the spectroscopic redshifts, luminosity-weighted ages, luminosity-weighted metallicities, and stellar masses given in the work by G05 for the subsample of 80 SDSS galaxies in common with ALHAMBRA and the photometric values determined from MUFFIT using the BC03 SSP models for the same galaxies and the ALHAMBRA data. The error bars at different parameter ranges indicate the typical 1σ uncertainties in the parameters from both methods. Different colours indicate different extinction ranges ($A_V < 0.3$; $0.3 \leq A_V < 0.6$; $A_V > 0.6$), as inferred from our code. In addition, to discuss aperture effects (SDSS spectra were taken in a 3″ aperture, while ALHAMBRA photo-spectra are not restricted to a fixed aperture, which is determined by the synthetic band *F814W*), star-shape markers are assigned to galaxies with apertures below 4″ in ALHAMBRA, which are, a priori, less affected by any potential aperture bias.

Except for two galaxies, which have been removed from the plots since their ALHAMBRA photometry has been confirmed to be affected by nearby and bright stars, the spectroscopic redshifts in Fig. 16a show excellent agreement with our photo-z, with an rms of $\sim$ 0.008. As we expect from Sect. 4.3, we rule out that any difference in the stellar populations between the two sources can be due to uncertainties in the photo z (see Sect. 4.4).

Concerning the luminosity-weighted age comparison, in Fig. 16b we find good qualitative agreement between both methods given the uncertainties of both methods (see black crosses in Fig. 16), in the sense that lower (higher) spectroscopic ages correspond, respectively, with lower (higher) photometric ages from MUFFIT. Interestingly, according to MUFFIT, young galaxies also tend to be more reddened by dust than old galaxies. From our results in this test sample, the mean age (luminosity-weighted) of the dusty galaxies ($A_V > 0.6$) is 1.8 Gyr, increasing to 3.9 Gyr for the intermediate extinction range and rising up to 5.4 Gyr for galaxies for which we retrieve low dust contents ($A_V \leq 0.3$). This is an expected result, since it is well known that younger galaxies may still have remnants of gas and dust from recent star formation events, whereas older/quiescent galaxies use to have less dust content.

We notice that this trend could in principle be explained by the age-extinction degeneracy (Sect. 4.5). However, if this were the case we would not find any qualitative relation with the spectroscopic ages, because the line indices, by construction, are not significantly affected by extinction. In addition, we emphasize that the galaxies in ALHAMBRA for which MUFFIT retrieves young stellar populations, for ages down to 2.6 Gyr, are also classified as *STARFORMING* in SDSS. This also supports the idea that the retrieved extinctions with MUFFIT are very robust and that they are not dominated by the degeneracy with age, because star-forming galaxies may present young populations with significant amounts of dust. In fact, previous and similar work (e.g. Fontana et al. 2006; Pozzetti et al. 2007; Ilbert et al. 2010) assumed in their codes that models with large extinctions are only allowed for star-forming galaxies. The key point from this result is that MUFFIT is able to intrinsically retrieve the extinction of the stellar populations without assuming any prior on the models or the galaxy type. Despite the qualitative agreement between MUFFIT and spectroscopic ages, with an rms of $\sim$1.6 Gyr, we also notice an offset between the ages of the two samples,

with the spectroscopic ages being ∼2 Gyr older than the ones derived from our code for the ALHAMBRA data. We discuss possible reasons for this offset at the end of this section.

In Fig. 16c we can see that the metallicities present qualitatively good agreement (despite the metallicity being more affected by uncertainties, see black crosses in Fig. 16), with an rms of ∼0.22 dex, although there is also a very small shift in the sense that our retrieved metallicities in ALHAMBRA tend to be smaller (Δ[Fe/H] ~ -0.08 dex) than the spectroscopic ones derived for SDSS galaxies in G05. It is noticeable that the metallicities of ALHAMBRA galaxies within an aperture of 4″ (star-shape markers) present better agreement with the spectroscopic measurements (Δ[Fe/H] $\lesssim -0.05$ dex) than the galaxies with larger apertures (dot markers; Δ[Fe/H] ~ -0.15 dex). As shown in G05, aperture effects and typical metallicity gradients can lead to up to ∼0.15–0.20 dex differences in metallicity for galaxies with $\gtrsim 10^{10}$ $M_{\odot}$. This reinforces the consistency and good agreement between both metallicity predictions (from SDSS and ALHAMBRA), since MUFFIT retrieves lower metallicities on average with respect to SDSS, and not higher, with a similar difference to those measured by G05 (∼0.17 dex) owing to possible aperture effects.

Interestingly, as pointed out by G05, a signal-to-noise ratio greater than 20 is required for a reliable constraint on the metallicity in SDSS spectra. Unfortunately, the adopted signal-to-noise ratio limit substantially restricts our sample, by excluding low-luminosity galaxies with potential sub-solar metallicities. Moreover, in G05 it is also mentioned that low-metallicity galaxies are more affected by uncertainties coming from their weak absorption features of [Mg_2Fe] and [MgFe]′. Indeed, in our subsample, the lower the metallicity, the greater the dispersion in the spectroscopic metallicity, as illustrated by the error bars. Instead, the metallicities provided by MUFFIT using ALHAMBRA data at the same regime are slightly better constrained, because in the end, it is the overall stellar continuum that mainly determines the retrieved stellar populations.

Figure 16d exhibits good agreement between the stellar masses of the two methods, with an rms of ∼0.19 dex, even with an offset of ∼0.18 dex. This offset in the stellar mass can be explained mainly by the systematic differences of ∼2 Gyr between the ages of both methods, since this implies a shift in the mass-luminosity relation in the sense that older galaxies, at the same apparent magnitude, are also more massive galaxies.

Before concluding, we intend to investigate the potential origin of the ∼2 Gyr offset in age derived in Fig. 16b. There are several potential reasons that could explain this offset: i) the age-extinction degeneracy; ii) the way to compute luminosity-weighted ages; iii) aperture effects; and iv) intrinsic systematic differences between both analysis techniques.

i) Unlike SED fitting techniques, absorption line-strength indices are basically not sensitive to extinction, because they are defined in short wavelength ranges. If the ages derived from MUFFIT were severely affected by the age-extinction degeneracy, we would expect galaxies with very low extinction values, $A_V < 0.05$, to present better agreement in the age comparison of Fig. 16b. However, this is not the case. By exploring the ages and metallicities of the galaxies with low extinction values ($A_V < 0.05$, according to MUFFIT and the ALHAMBRA data), checking that both metallicities, spectroscopic and photometric, remain in agreement without great differences, we find that the age difference is still ∼2 Gyr. This rejects the potential impact of the age-metallicity degeneracy, as well as the influence of using different extinction laws.

ii) In G05, luminosity-weighted ages are computed according to the total *r*-band flux, whereas in MUFFIT this is done using the whole flux in all the ALHAMBRA bands. To explore whether this normalisation difference could drive the age offset, we recomputed the MUFFIT luminosity-weighted ages using the ALHAMBRA *F644W* band, which has the most similar effective wavelength to the SDSS *r*-band. The results are essentially the same, so do not explain the observed age offset.

iii) It is well known that early-type galaxies may show radial variations in their stellar population properties, showing gradients in metallicity and/or age. We already discussed above how the combination of different photometric apertures and the existence of metallicity gradients has an impact on the metallicity comparison of Fig. 16c). It is worth noting, however, that age gradients generally used to be shallower than metallicity gradients (Wu et al. 2005; Sánchez-Blázquez et al. 2007; La Barbera et al. 2012; Eigenthaler & Zeilinger 2013), so aperture effects are expected to be less as well. Nevertheless, shallow gradients in all the parameters can also be found (González Delgado et al. 2015). To assess this effect, we focus on galaxies whose photometric apertures in ALHAMBRA are down to 4″ (Fig. 16), not far from the SDSS fibre aperture. We observe that the age offset is significant even for these galaxies, so aperture effects are rejected to explain the age offset, too.

iv) After the negative results of the three previous tests, the existence of intrinsic systematic differences between the two methods seems to be the most plausible reason for the different absolute values of the derived ages. The discrepancies between the analysis of spectral features versus colours, together with the assumptions of different SFHs (exponentially declining tau models in G05, versus a mixture of young+old SSPs in this work), may be responsible for the age offset. To shed light on this last item, we aim at constraining a purely mathematical problem: the potential differences between the luminosity ages derived from parametric τ-models and the ones derived from a non-parametric mixture of two SSPs. To do this, we made use of the set of τ-model *Synthetic Spectral Atlas of Galaxies* (SSAG, Magris et al. 2015), which is very similar to the τ models employed in G05. SSAG models are based on the recipes described in Chen et al. (2012) and have been constructed following exponentially declining SFH and BC03 models, which may randomly suffer an instantaneous and random burst during different periods of time. The SSAG also includes intrinsic extinctions, following the dust model of Charlot & Fall (2000), and different velocity dispersions.

To create a subsample of RS galaxies, we selected all the SSAG galaxy models whose colours satisfy $U - V \gtrsim 2.0$ (AB-system). After convolving SSAG models with the ALHAMBRA filter set, we ran MUFFIT using the same BC03 models as input, in concordance with SSAG, and compared derived luminosity-weighted ages with the input SSAG ones. The result of the comparison is exhibited in Fig. 17. There appears to be a systematic offset between ages of $\Delta\mathrm{Age_L} \sim 1.8 \pm 1.7$ Gyr, which fully explains (qualitatively and quantitatively) the $\sim 2 \pm 1.6$ Gyr offset found in the previous comparison between the spectroscopic ages of G05 and the ones retrieved using MUFFIT and ALHAMBRA data, as due to the mathematical differences

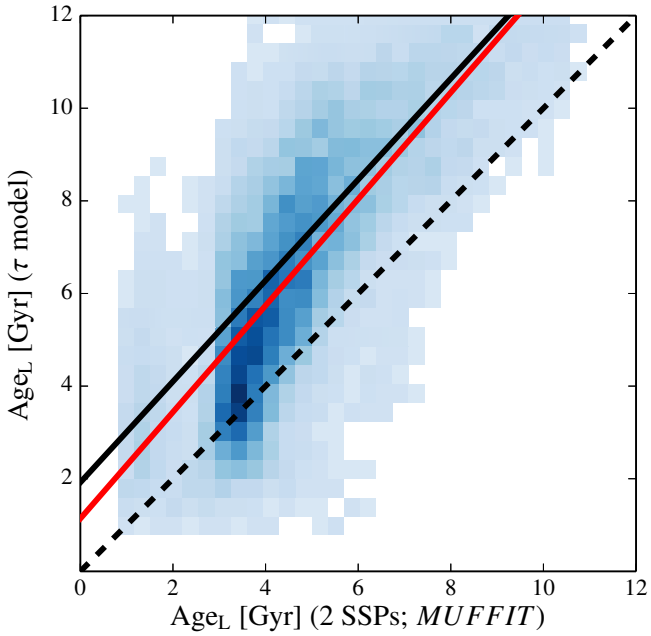

Fig. 17. Comparison between the luminosity-weighted ages of a subset of RS τ-models from SSAG and the ones derived by MUFFIT for the same models employing a mixture of 2 SSPs. The dashed black line represents the one-to-one relationship, while the red line is the simple linear regression of the data points. The solid black line illustrates the fit between the ages provided by G05 and the ones provided by MUFFIT using ALHAMBRA data (see Fig. 16b).

in the diagnostic input models (mixture of SSP models vs. exponentially declining SFH models).

Finally, we have also investigated the impact of using a different set of SSP models for the stellar population comparison. In Fig. 18 we present the same comparison of Fig. 16, but in this case having used the MIUSCAT SSP models, instead of BC03, to analyse the ALHAMBRA data with MUFFIT. Except for a slightly larger difference in metallicity, in the sense that MIUSCAT models tend to predict lower metallicities, the rest of the parameters are similar to Fig. 16. This is important for assessing the impact of different SSP models on the absolute values of the derived parameters.

6. Summary and conclusions

The arrival of present and future large-scale multi-filter surveys (e.g. COMBO-17, COSMOS, ALHAMBRA, SHARDS, J-PLUS, and J-PAS) promises that formidable datasets for many purposes in Cosmology and Astrophysics will be available. These photometric surveys, based on the mapping of different regions of the sky with a set of contiguous intermediate- and narrow-band filters, provide low-resolution photo spectra for each region of the sky (hence performing like a low-resolution IFU with PSF-limited spatial resolution), with the survey depth as the only selection criterion and without the typical spectroscopic uncertainties in the flux calibration. This opens an unprecedented way to progress in our understanding about galaxy evolution through studying millions of homogeneous galaxy SEDs, both spatially resolved in the closer Universe and integrated.

This paper was devoted to presenting MUFFIT (MUlti-Filter FITting for stellar population diagnostics), a generic code specifically designed to analyse the stellar content of galaxies with available multi-filter data (dealing with the technical peculiarities and the big amount of high-quality photometric data available in multi-filter surveys), as well as to show its functionalities, set the accuracy and typical uncertainties in the retrieved stellar population parameters, and ultimately test it with real data. In this way, we made use of the ALHAMBRA database as a test bench for MUFFIT, not with the aim of performing a thorough stellar population analysis of the galaxies in ALHAMBRA (which constitutes the matter of the next papers in this series), but to compare the stellar population results derived from MUFFIT with similar studies in the literature, allowing us to assess its reliability and the feasibility of this kind of technique to accurately explore the stellar content of galaxies.

In the following items the main conclusions of this work are summarised:

- Using a set of SSP models that explores different stellar population parameters as input, MUFFIT builds photometric predictions of bands at different redshifts and extinctions. For the present work, the stellar population parameters that were considered are only age and metallicity, although in a general case even the IMF slope and the α-enhancement can also be retrieved if SSP models properly account for them. In addition, the survey photometry was corrected for MW dust effects, as the colour terms introduced by MW dust may play an important role not only in the stellar masses derived using SED-fitting techniques, but also in the retrieved stellar population parameters.
- MUFFIT compares the multi-filter fluxes of a given galaxy with the photometric predictions of a reasonable mixture of two SSPs, one younger and one older than the mean age provided by a single SSP fitting. The mixture of two SSPs determined by the last prior, specific for each individual galaxy, is a relevant improvement over the fitting of only one SSP, since it represents an underlying main red population plus a less massive and later episode of star formation. The stellar population parameters provided by MUFFIT (in this work the age and metallicity weighted by both luminosity and mass, extinction, redshift, and stellar mass) are constrained by the use of an error-weighted χ^2 test. During the fitting process, MUFFIT removes those bands that are affected by emission lines, improving the quality of the fitting and restricting the plausible redshift space, as in a general case the redshift of the galaxy is treated as another free parameter to be determined. MUFFIT is not limited to providing the parameters of the best-fitting model, but also explores the parameter space using the proper photometric uncertainties in each band by a Monte Carlo method, reinforcing the parameter predictions because it provides their statistical uncertainties, too. MUFFIT also computes and provides the k corrections of each galaxy from the same mixture of models in rest frame.
- Specifically for the ALHAMBRA data, we studied the intrinsic uncertainties in redshift, extinction, age, metallicity, and stellar mass that appear when diagnosed by MUFFIT. Using the typical distribution of errors for the RS galaxies in ALHAMBRA, we constructed mock galaxies with an average S/N per filter of 20, obtaining typical uncertainties (rms) of $\sigma_z \sim 0.01$, $\sigma_{A_V} \sim 0.11$, $\sigma_{\rm Age} \sim 0.10$ dex, $\sigma_{\rm [Fe/H]} \sim 0.16$ dex, and $\sigma_{M_\star} \sim 0.08$ dex. In no case were there systematic errors that are statistically significant.
- Even though MUFFIT is not a generic photo-z code, using the redshift PDFs provided by external photo-z codes as input, MUFFIT returns fine-tuned redshift values whose

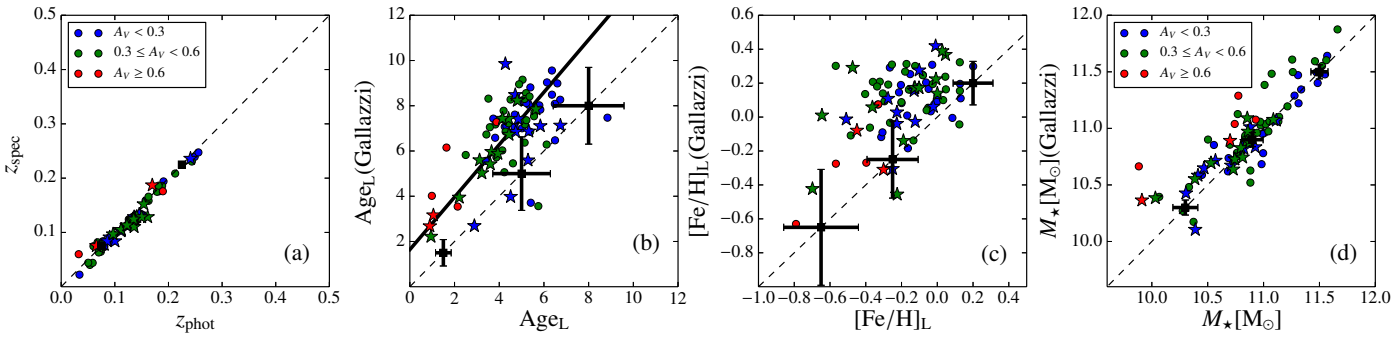

Fig. 18. As in Fig. 16 but using the MIUSCAT SSP models instead of the BC03 ones.

accuracy is improved by ∼10–20%. We also found that the photo-z accuracy reached in ALHAMBRA, $\sigma_{NMAD} \lesssim 0.009$, has a negligible impact on the main stellar population parameters retrieved using MUFFIT, where the typical uncertainties in the photometry are more crucial.

- We studied the age-metallicity-extinction degeneracy of the ALHAMBRA data with MUFFIT at different parameter ranges, after having fixed the IMF slope. The age-extinction anti-correlation is present in all ranges of age and metallicity. However, the well known age-metallicity anti-correlation may turn into a positive correlation for young and/or metal-poor populations due to the role of the extinction in reddening the spectral energy distributions of galaxies.
- The stellar-mass predictions provided by MUFFIT for a common sample of RS galaxies in ALHAMBRA are in wonderful agreement with the stellar masses computed for the same galaxies in COSMOS. The dispersion of the comparison, with an rms of $\Delta \log_{10} M_\star \sim 0.15$ dex, can be fully explained by the intrinsic uncertainties of both methods.
- MUFFIT offers a reliable way to explore emission lines in multi-filter surveys. Using a set of emission line galaxies shared by SDSS and ALHAMBRA, we demonstrate that the residuals provided by MUFFIT for the filters affected by emission lines in ALHAMBRA are correlated with the strengths of the main emission lines.
- The age-metallicity loci provided by MUFFIT for a sample of $z \leq 0.22$ early-type galaxies in ALHAMBRA in different stellar mass bins are in very good agreement with the ones determined from SDSS data on the basis of spectroscopic diagnostics. When we analysed the stellar content of these galaxies in ALHAMBRA using their photometric data and MUFFIT, our results showed that the more massive early types ($\gtrsim 10^{11} M_\star[M_\odot]$) were formed in an earlier epoch than their low-mass counterparts ($\lesssim 10^{10} M_\star[M_\odot]$) with a larger content of metals with differences of ΔAge $\sim$ 3 Gyr and Δ[Fe/H] $\sim$ 0.3 dex. This result agrees with the "downsizing" scenario as well.
- For a subsample of galaxies shared by ALHAMBRA and SDSS, a one-to-one comparison between the redshifts, ages, metallicities, and stellar masses derived spectroscopically for the SDSS data (provided by Gallazzi et al. 2005) and those determined from MUFFIT and ALHAMBRA reveal good qualitative agreement in all the parameters given the uncertainties of both methods, with typical rms for the distribution of differences between both diagnostics of $\sigma_z^{SDSS} \sim 0.008$, $\sigma_{Age}^{SDSS} \sim 1.6$ Gyr, $\sigma_{[Fe/H]}^{SDSS} \sim 0.2$ dex, and $\sigma_{M_\star}^{SDSS} \sim 0.19$ dex, thus reinforcing the strengths of multi-filter galaxy data and optimised analysis techniques, like MUFFIT, to conduct reliable stellar population studies. Despite the qualitative agreement between ages, in the sense that young (old) spectroscopic ages in SDSS are also found to be young (old) photometric ages in ALHAMBRA using MUFFIT, there is a systematic difference of ∼2 Gyr between the two samples that is explained by the differences between using mixtures of SSPs instead of τ models. And even though there is good agreement between metallicities, it is noticeable that the metallicities of ALHAMBRA galaxies within an aperture of $\leq 4''$ offer better agreement with the spectroscopic measurements (Δ[Fe/H] $\lesssim$ 0.05 dex) than the galaxies with larger apertures (Δ[Fe/H] $\lesssim$ 0.15 dex), pointing towards the possibility that aperture differences between SDSS and ALHAMBRA and the existence of metallicity gradients drive the observed differences (in agreement with G05). There is also good agreement between stellar masses, with a minor shift of ∼0.18 dex that can be explained by the observed offset in age.

To conclude, we demonstrate that MUFFIT is a reliable stellar population code for multi-filter galaxy data, which is suited to and optimized for analysing the stellar content of galaxies in ALHAMBRA-like surveys. This opens a new way to explore and address stellar population studies of galaxies with multiple photometric bands or colours, as long as the effective spectral resolution is at least the one of ALHAMBRA, allowing us to accurately extract the stellar content of thousands of galaxies at higher redshifts, benefited by the large-number statistics in comparison with typical spectroscopic datasets at the same redshift. With the arrival of the new-generation large-scale multi-filter surveys, such as J-PLUS and J-PAS, codes like MUFFIT will contribute to shedding light on our understanding of the formation and evolution of galaxies.

Acknowledgements. We thank the referee for the valuable suggestions and comments that reinforced part of our results. L.A.D.G. acknowledges support from the "Caja Rural de Teruel" for developing this research. A.J.C. is a Ramón y Cajal Fellow of the Spanish Ministry of Science and Innovation. This work has been supported by the "Programa Nacional de Astronomía y Astrofísica" of the Spanish Ministry of Economy and Competitiveness (MINECO) under grant AYA2012-30789, as well as by FEDER funds and the Government of Aragón, through the Research Group E103. L.A.D.G. also thanks the Mullard Space Science Laboratory (MSSL) and Royal Astronomical Society (RAS) for offering the opportunity to support and develop part of this research in collaboration with I.F. MINECO grants AYA2010-15081, AYA2010-15169, AYA2010-22111-C03-01, AYA2010-22111-C03-02, AYA2011-29517-C03-01, AYA2013-40611-P, AYA2013-42227-P, AYA2013-43188-P, AYA2013-48623-C2-1, AYA2013-48623-C2-2, and AYA2014-58861-C3-1 are also acknowledged, together with Generalitat Valenciana projects Prometeo 2009/064 and PROMETEOII/2014/060, and Junta de Andalucía grants TIC114, JA2828, and P10-FQM-6444. MP acknowledges financial support from the JAE-Doc programme of the Spanish National Research Council (CSIC), co-funded by the European Social Fund. The Max Planck Institute for Astrophysics

and the Johns Hopkins University are acknowledged for making their catalogues (MPA/JHU catalogues) publicly available with the physical properties for galaxies in SDSS employed in this work. Throughout this research, we made use of the `Matplotlib` package (Hunter 2007), a 2D graphics package used for `Python` which is designed for interactive scripting and quality image generation.

References

Abazajian, K. N., Adelman-McCarthy, J. K., Agüeros, M. A., et al. 2009, ApJS, 182, 543
Adelman-McCarthy, J. K., Agüeros, M. A., Allam, S. S., et al. 2006, ApJS, 162, 38
Aparicio Villegas, T., Alfaro, E. J., Cabrera-Caño, J., et al. 2010, AJ, 139, 1242
Arnouts, S., Moscardini, L., Vanzella, E., et al. 2002, MNRAS, 329, 355
Arnouts, S., Le Floc'h, E., Chevallard, J., et al. 2013, A&A, 558, A67
Baldry, I. K., Glazebrook, K., Brinkmann, J., et al. 2004, ApJ, 600, 681
Balogh, M. L., Morris, S. L., Yee, H. K. C., Carlberg, R. G., & Ellingson, E. 1999, ApJ, 527, 54
Baum, W. A. 1959, PASP, 71, 106
Bell, E. F., Wolf, C., Meisenheimer, K., et al. 2004, ApJ, 608, 752
Benítez, N., Moles, M., Aguerri, J. A. L., et al. 2009, ApJ, 692, L5
Benitez, N., Dupke, R., Moles, M., et al. 2014, in Highlights of Spanish Astrophysics VIII, Proc. XI Scientific Meeting of the Spanish Astronomical Society held on September 8-12, 2014, in Teruel, Spain, eds. A. J. Cenarro, F. Figueras, C. Hernández-Monteagudo, J. Trujillo Bueno, & L. Valdivielso, 148
Bernardi, M., Nichol, R. C., Sheth, R. K., Miller, C. J., & Brinkmann, J. 2006, AJ, 131, 1288
Bessell, M. S. 2005, ARA&A, 43, 293
Bolzonella, M., Miralles, J.-M., & Pelló, R. 2000, A&A, 363, 476
Brammer, G. B., van Dokkum, P. G., & Coppi, P. 2008, ApJ, 686, 1503
Brinchmann, J., Charlot, S., White, S. D. M., et al. 2004, MNRAS, 351, 1151
Bruzual, G., & Charlot, S. 2003, MNRAS, 344, 1000
Burstein, D., Faber, S. M., Gaskell, C. M., & Krumm, N. 1984, ApJ, 287, 586
Calzetti, D. 1997, in AIP Conf. Ser. 408, ed. W. H. Waller, 403
Calzetti, D., Armus, L., Bohlin, R. C., et al. 2000, ApJ, 533, 682
Cardelli, J. A., Clayton, G. C., & Mathis, J. S. 1989, ApJ, 345, 245
Cassata, P., Guzzo, L., Franceschini, A., et al. 2007, ApJS, 172, 270
Cenarro, A. J., Cardiel, N., Gorgas, J., et al. 2001a, MNRAS, 326, 959
Cenarro, A. J., Gorgas, J., Cardiel, N., et al. 2001b, MNRAS, 326, 981
Cenarro, A. J., Gorgas, J., Cardiel, N., Vazdekis, A., & Peletier, R. F. 2002, MNRAS, 329, 863
Cenarro, A. J., Peletier, R. F., Sánchez-Blázquez, P., et al. 2007, MNRAS, 374, 664
Cervantes, J. L., & Vazdekis, A. 2009, MNRAS, 392, 691
Chabrier, G. 2003, PASP, 115, 763
Charlot, S., & Fall, S. M. 2000, ApJ, 539, 718
Chen, Y.-M., Kauffmann, G., Tremonti, C. A., et al. 2012, MNRAS, 421, 314
Cid Fernandes, R., Mateus, A., Sodré, L., Stasińska, G., & Gomes, J. M. 2005, MNRAS, 358, 363
Coelho, P., Mendes de Oliveira, C., & Cid Fernandes, R. 2009, MNRAS, 396, 624
Conroy, C., & van Dokkum, P. 2012, ApJ, 747, 69
Cooper, M. C., Aird, J. A., Coil, A. L., et al. 2011, ApJS, 193, 14
Cowie, L. L., Songaila, A., Hu, E. M., & Cohen, J. G. 1996, AJ, 112, 839
Cristóbal-Hornillos, D., Aguerri, J. A. L., Moles, M., et al. 2009, ApJ, 696, 1554
Davis, M., Guhathakurta, P., Konidaris, N. P., et al. 2007, ApJ, 660, L1
Eigenthaler, P., & Zeilinger, W. W. 2013, A&A, 553, A99
Faber, S. M. 1973, ApJ, 179, 731
Faber, S. M., Friel, E. D., Burstein, D., & Gaskell, C. M. 1985, ApJS, 57, 711
Faber, S. M., Willmer, C. N. A., Wolf, C., et al. 2007, ApJ, 665, 265
Falcón-Barroso, J., Sánchez-Blázquez, P., Vazdekis, A., et al. 2011, A&A, 532, A95
Ferreras, I., & Silk, J. 2000, ApJ, 541, L37
Ferreras, I., La Barbera, F., de la Rosa, I. G., et al. 2013, MNRAS, 429, L15
Fitzpatrick, E. L. 1999, PASP, 111, 63
Fontana, A., Salimbeni, S., Grazian, A., et al. 2006, A&A, 459, 745
Fritz, A., Scodeggio, M., Ilbert, O., et al. 2014, A&A, 563, A92
Gallazzi, A., Charlot, S., Brinchmann, J., White, S. D. M., & Tremonti, C. A. 2005, MNRAS, 362, 41
Gallazzi, A., Charlot, S., Brinchmann, J., & White, S. D. M. 2006, MNRAS, 370, 1106
Gawiser, E., van Dokkum, P. G., Herrera, D., et al. 2006, ApJS, 162, 1
González Delgado, R. M., Cerviño, M., Martins, L. P., Leitherer, C., & Hauschildt, P. H. 2005, MNRAS, 357, 945
González Delgado, R. M., García-Benito, R., Pérez, E., et al. 2015, A&A, 581, A103
Gorgas, J., Faber, S. M., Burstein, D., et al. 1993, ApJS, 86, 153
Gorgas, J., Jablonka, P., & Goudfrooij, P. 2007, A&A, 474, 1081
Heap, S. R., & Lindler, D. J. 2007, in From Stars to Galaxies: Building the Pieces to Build Up the Universe, eds. A. Vallenari, R. Tantalo, L. Portinari, & A. Moretti, ASP Conf. Ser., 374, 409
Hogg, D. W. 1999, ArXiv e-prints [arXiv:astro-ph/9905116]
Huertas-Company, M., Rouan, D., Tasca, L., Soucail, G., & Le Fèvre, O. 2008, A&A, 478, 971
Hunter, J. D. 2007, Computing In Science & Engineering, 9, 90
Ilbert, O., Arnouts, S., McCracken, H. J., et al. 2006, A&A, 457, 841
Ilbert, O., Capak, P., Salvato, M., et al. 2009, ApJ, 690, 1236
Ilbert, O., Salvato, M., Le Floc'h, E., et al. 2010, ApJ, 709, 644
Jimenez, R., Bernardi, M., Haiman, Z., Panter, B., & Heavens, A. F. 2007, ApJ, 669, 947
Johnson, H. L., & Morgan, W. W. 1953, ApJ, 117, 313
Jørgensen, I. 1999, MNRAS, 306, 607
Kaviraj, S., Schawinski, K., Devriendt, J. E. G., et al. 2007, ApJS, 173, 619
Koleva, M., Prugniel, P., Ocvirk, P., Le Borgne, D., & Soubiran, C. 2008, MNRAS, 385, 1998
Koleva, M., Prugniel, P., Bouchard, A., & Wu, Y. 2009, A&A, 501, 1269
Kriek, M., van Dokkum, P. G., Labbé, I., et al. 2009, ApJ, 700, 221
Kroupa, P. 2001, MNRAS, 322, 231
Kuntschner, H., Lucey, J. R., Smith, R. J., Hudson, M. J., & Davies, R. L. 2001, MNRAS, 323, 615
La Barbera, F., Ferreras, I., de Carvalho, R. R., et al. 2012, MNRAS, 426, 2300
Le Borgne, J.-F., Bruzual, G., Pelló, R., et al. 2003, A&A, 402, 433
Lilly, S. J., Le Fèvre, O., Renzini, A., et al. 2007, ApJS, 172, 70
Lilly, S. J., Le Brun, V., Maier, C., et al. 2009, ApJS, 184, 218
Liu, G., Lu, Y., Chen, X., Du, W., & Zhao, Y. 2013, ArXiv e-prints [arXiv:1305.2984]
Lonoce, I., Longhetti, M., Saracco, P., Gargiulo, A., & Tamburri, S. 2014, MNRAS, 444, 2048
Magris C., G., Mateu P., J., Mateu, C., et al. 2015, PASP, 127, 16
Maraston, C., Strömbäck, G., Thomas, D., Wake, D. A., & Nichol, R. C. 2009, MNRAS, 394, L107
Mármol-Queraltó, E., Cardiel, N., Cenarro, A. J., et al. 2008, A&A, 489, 885
Martins, L. P., González Delgado, R. M., Leitherer, C., Cerviño, M., & Hauschildt, P. 2005, MNRAS, 358, 49
Massa, D. 1987, AJ, 94, 1675
Mathis, H., Charlot, S., & Brinchmann, J. 2006, MNRAS, 365, 385
Mathis, J. S. 1990, ARA&A, 28, 37
McClure, R. D., & van den Bergh, S. 1968, AJ, 73, 313
Moles, M., Benítez, N., Aguerri, J. A. L., et al. 2008, AJ, 136, 1325
Molino, A., Benítez, N., Moles, M., et al. 2014, MNRAS, 441, 2891
Monachesi, A., Trager, S. C., Lauer, T. R., et al. 2012, ApJ, 745, 97
Ocvirk, P., Pichon, C., Lançon, A., & Thiébaut, E. 2006, MNRAS, 365, 74
O'Donnell, J. E. 1994, ApJ, 422, 158
Oke, J. B., & Gunn, J. E. 1983, ApJ, 266, 713
Pérez-González, P. G., Cava, A., Barro, G., et al. 2013, ApJ, 762, 46
Pickles, A., & Depagne, É. 2010, PASP, 122, 1437
Poggianti, B. M., Bridges, T. J., Carter, D., et al. 2001, ApJ, 563, 118
Postman, M., Coe, D., Benítez, N., et al. 2012, ApJS, 199, 25
Pović, M., Huertas-Company, M., Aguerri, J. A. L., et al. 2013, MNRAS, 435, 3444
Pozzetti, L., Bolzonella, M., Lamareille, F., et al. 2007, A&A, 474, 443
Prevot, M. L., Lequeux, J., Prevot, L., Maurice, E., & Rocca-Volmerange, B. 1984, A&A, 132, 389
Pritchet, C. 1977, ApJS, 35, 397
Prugniel, P., & Soubiran, C. 2001, A&A, 369, 1048
Ricciardelli, E., Vazdekis, A., Cenarro, A. J., & Falcón-Barroso, J. 2012, MNRAS, 424, 172
Rogers, B., Ferreras, I., Peletier, R., & Silk, J. 2010, MNRAS, 402, 447
Sánchez-Blázquez, P., Gorgas, J., Cardiel, N., & González, J. J. 2006a, A&A, 457, 809
Sánchez-Blázquez, P., Peletier, R. F., Jiménez-Vicente, J., et al. 2006b, MNRAS, 371, 703
Sánchez-Blázquez, P., Forbes, D. A., Strader, J., Brodie, J., & Proctor, R. 2007, MNRAS, 377, 759
Santos, F. C. Jr., J., Alloin, D., Bica, E., & Bonatto, C. J. 2002, in Extragalactic Star Clusters, eds. D. P. Geisler, E. K. Grebel, & D. Minniti, IAU Symp., 207, 727
Sawicki, M. 2012, PASP, 124, 1208
Schlafly, E. F., & Finkbeiner, D. P. 2011, ApJ, 737, 103
Schlegel, D. J., Finkbeiner, D. P., & Davis, M. 1998, ApJ, 500, 525
Scoville, N., Aussel, H., Brusa, M., et al. 2007, ApJS, 172, 1
Stone, R. P. S. 1996, ApJS, 107, 423
Strateva, I., Ivezić, Ž., Knapp, G. R., et al. 2001, AJ, 122, 1861
Thomas, D., Maraston, C., & Bender, R. 2003, MNRAS, 339, 897

Thomas, D., Maraston, C., Bender, R., & Mendes de Oliveira, C. 2005, ApJ, 621, 673
Tifft, W. G. 1963, AJ, 68, 302
Tojeiro, R., Heavens, A. F., Jimenez, R., & Panter, B. 2007, MNRAS, 381, 1252
Trager, S. C., Worthey, G., Faber, S. M., Burstein, D., & González, J. J. 1998, ApJS, 116, 1
Tremonti, C. A., Heckman, T. M., Kauffmann, G., et al. 2004, ApJ, 613, 898
Valdes, F., Gupta, R., Rose, J. A., Singh, H. P., & Bell, D. J. 2004, ApJS, 152, 251
Vazdekis, A., & Arimoto, N. 1999, ApJ, 525, 144
Vazdekis, A., Cenarro, A. J., Gorgas, J., Cardiel, N., & Peletier, R. F. 2003, MNRAS, 340, 1317
Vazdekis, A., Sánchez-Blázquez, P., Falcón-Barroso, J., et al. 2010, MNRAS, 404, 1639
Vazdekis, A., Ricciardelli, E., Cenarro, A. J., et al. 2012, MNRAS, 424, 157
Walcher, J., Groves, B., Budavári, T., & Dale, D. 2011, Ap&SS, 331, 1
Williams, R. J., Quadri, R. F., Franx, M., van Dokkum, P., & Labbé, I. 2009, ApJ, 691, 1879
Wolf, C., Meisenheimer, K., Rix, H.-W., et al. 2003, A&A, 401, 73
Wood, D. B. 1966, ApJ, 145, 36
Worthey, G. 1994, ApJS, 95, 107
Worthey, G., Faber, S. M., Gonzalez, J. J., & Burstein, D. 1994, ApJS, 94, 687
Wu, H., Shao, Z., Mo, H. J., Xia, X., & Deng, Z. 2005, ApJ, 622, 244

[1] Centro de Estudios de Física del Cosmos de Aragón (CEFCA), Plaza San Juan 1, Floor 2, 44001 Teruel, Spain
e-mail: diaz@cefca.es
[2] Mullard Space Science Laboratory, University College London, Holmbury St Mary, Dorking, Surrey RH5 6NT, UK
[3] IAA-CSIC, Glorieta de la Astronomía s/n, 18008 Granada, Spain
[4] Observatori Astronòmic, Universitat de València, C/ Catedràtic José Beltrán 2, 46980 Paterna, Spain
[5] GEPI, Observatoire de Paris, CNRS, Université Paris Diderot, 61, Avenue de l'Observatoire 75014, Paris France
[6] Instituto de Astrofísica de Canarias, vía Láctea s/n, 38200 La Laguna, Tenerife, Spain
[7] Departamento de Astrofísica, Facultad de Física, Universidad de La Laguna, 38206 La Laguna, Spain
[8] Instituto de Astronomía, Geofísica e Ciéncias Atmosféricas, Universidade de São Paulo, São Paulo, Brazil
[9] Observatório Nacional-MCT, Rua José Cristino, 77, CEP 20921-400, Rio de Janeiro-RJ, Brazil
[10] Department of Theoretical Physics, University of the Basque Country UPV/EHU, 48080 Bilbao, Spain
[11] IKERBASQUE, Basque Foundation for Science, 48013 Bilbao, Spain
[12] Departamento de Física Atómica, Molecular y Nuclear, Facultad de Física, Universidad de Sevilla, 41012 Sevilla, Spain
[13] Institut de Ciències de l'Espai (IEEC-CSIC), Facultat de Ciències, Campus UAB, 08193 Bellaterra, Spain
[14] Instituto de Física de Cantabria (CSIC-UC), 39005 Santander, Spain
[15] Unidad Asociada Observatorio Astronómico (IFCA-UV), 46980 Paterna, Spain
[16] Departamento de Astronomía, Pontificia Universidad Católica, 782-0436 Santiago, Chile
[17] Departament d'Astronomia i Astrofísica, Universitat de València, 46100 Burjassot, Spain
[18] Instituto de Física Teórica, (UAM/CSIC), Universidad Autónoma de Madrid, Cantoblanco, 28049 Madrid, Spain
[19] Campus of International Excellence UAM+CSIC, Cantoblanco, 28049 Madrid, Spain
[20] Department of Mechanical Engineering and INSIGNEO Institute for in silico Medicine, University of Sheffield, UK